



(A New Proposal to Jefferson Lab 12 GeV - PAC34)  
**Measurement of the Semi-Inclusive  $\pi$  and  $K$   
electro-production in DIS regime from transversely  
polarized  $^3\text{He}$  target with the SBS & BB  
spectrometers in Hall A**

G. Cates(spokesperson), H. Baghdasaryan, D. Day, P. Dolph,  
N. Kalantarians, R. Lindgren, N. Liyanage, V. Nelyubin, S. Riordan, Al Tobias  
*University of Virginia, Charlottesville, VA 22901*

E. Cisbani(spokesperson), F. Cusanno, F. Garibaldi, S. Frullani, G. M. Urciuoli, F. Meddi  
*INFN, Rome and gruppo collegato Sanità and University "La Sapienza", Rome, Italy*

G.B. Franklin(spokesperson), B. Quinn, R. Schumacher  
*Carnegie Mellon University, Pittsburgh, PA 15213*

B. Wojtsekhowski (contact and spokesperson), A. Camsonne, E. Chudakov,  
P. Degtyarenko, M. Jones, J. Gomez, O. Hansen, D. W. Higinbotham,  
J. LeRose, R. Michaels, S. Nanda, A. Saha, V. Sulkovsky  
*Thomas Jefferson National Accelerator Facility, Newport News, VA 23606*

J. Annand, D. Hamilton, D. Ireland, R. Kaiser, K. Livingston,  
I. MacGregor, B. Seitz, and G. Rosner  
*University of Glasgow, Glasgow, Scotland*

W. Boeglin, P. Markowitz, J. Reinhold      T. Averett, L.P. Pentchev, C.F. Perdrisat  
*Florida International University, Fl*                      *College of William and Mary*

V. Punjabi, M. Khandaker      D. Nikolenko, I. Rachek, Yu. Shestakov  
*Norfolk State University*                      *Budker Institute, Novosibirsk, Russia*

R. De Leo, L. Lagamba, S. Marrone, G. Simonetti, E. Nappi, I. Vilaridi  
*INFN, Bari and Univeristy of Bari, Italy*

V. Bellini, A. Giusa, F. Mammoliti, C. Randieri, G. Russo,  
M.L. Sperduto, C.M. Sutura  
*INFN Catania and University of Catania, Catania, Italy*

E. De Sanctis, L. Hovsepyan, M. Mirazita, S.A. Pereira, P. Rossi  
*INFN, Laboratori Nazionali di Frascati, Frascati, Italy*

A. D'Angelo  
*INFN Rome2 and University "Tor Vergata", Rome, Italy*

M. Battaglieri, R. De Vita, V. Drozdov, M. Osipenko, M. Ripani, M. Taiuti  
*INFN Genova and University of Genova, Genoa, Italy*

P.F. Dalpiaz, G. Ciullo, M. Contalbrigo, F. Giordano, P. Lenisa, L. Pappalardo  
*INFN Ferrara and University of Ferrara, Ferrara, Italy*

J. Lichtenstadt, I. Pomerantz, E. Piasetzky, G. Ron  
*Tel Aviv University, Israel*

A. Glamazdin  
*Kharkov Institute of Physics and Technology, Kharkov 310077, Ukraine*

J. Calarco, K. Slifer  
*University of New Hampshire, Durham, NH 03824*

W. Bertozzi, S. Gilad  
*Massachusetts Institute of Technology, Cambridge, MA 02139*

B. Vlahovic  
*North Carolina Central University, Durham, NC 03824*

A. Sarty  
*Saint Mary's University, Nova Scotia, Canada B3H 3C3*

K. Aniol and D. J. Magaziotis  
*Cal State University, Los Angeles, CA 90032*

S. Abrahamyan, S. Mayilyan, A. Shahinyan, H. Voskanyan  
*Yerevan Physics Institute, Yerevan, Armenia*

December 15, 2008

# Contents

<b>1</b>	<b>Partonic Structure of the Nucleon</b>	<b>1</b>
1.1	Deep Inelastic Scattering . . . . .	2
1.2	Transversity . . . . .	5
1.3	Spin-orbit effects and the FSI in nuclear physics . . . . .	7
1.4	Transverse momentum physics and an impact parameter at large $Q^2$ . . . . .	8
1.5	Experimental and theoretical status . . . . .	9
<b>2</b>	<b>Proposed Measurements</b>	<b>12</b>
2.1	Overview . . . . .	12
2.2	Physics Goals . . . . .	13
2.3	Kinematics . . . . .	14
2.4	Systematics . . . . .	15
<b>3</b>	<b>Experimental Setup</b>	<b>16</b>
3.1	CEBAF polarized beam . . . . .	16
3.2	Super Bigbite Spectrometer . . . . .	17
3.2.1	Counting Rates of the Super BigBite Detectors . . . . .	23
3.3	BigBite Spectrometer . . . . .	23
3.3.1	Counting Rates of the BigBite Detectors . . . . .	24
3.4	Logic of the Trigger and DAQ rate . . . . .	25
<b>4</b>	<b>The Polarized <math>^3\text{He}</math> Target</b>	<b>27</b>
4.1	The principles behind the GEN-II target . . . . .	29
4.2	The GEN-I polarized $^3\text{He}$ target and subsequent studies. . . . .	31
4.3	The GEN-II High-Luminosity Target Cell . . . . .	33
4.4	Convection Tests in a Prototype GEN-II Target Cell . . . . .	36
4.5	Choosing Design Parameters for the GEN-II High-Luminosity Target . . . . .	39
4.6	The Physical Configuration of the GEN-II Target . . . . .	39
<b>5</b>	<b>Data Production and Analysis</b>	<b>41</b>
5.1	(SI)DIS Event Selection . . . . .	41
5.2	Phase Space . . . . .	41
5.3	Asymmetries . . . . .	43
5.4	Rates . . . . .	49

5.5	Extraction of the Sivers and Collins Asymmetries . . . . .	56
5.6	Systematics Errors Analysis . . . . .	56
5.6.1	Target related effects . . . . .	58
5.6.2	Random background . . . . .	58
5.6.3	Exclusive Vector Meson production . . . . .	58
5.6.4	Hadron Identification . . . . .	58
5.6.5	Additional azimuthal modulated terms . . . . .	59
5.6.6	Acceptance effects . . . . .	60
5.6.7	Study of additional systematics in the analysis . . . . .	60
5.7	$A_{UT}$ Predictions . . . . .	60
<b>6</b>	<b>Summary</b>	<b>65</b>
<b>A</b>	<b>Collaboration responsibilities</b>	<b>67</b>

## Abstract

An experiment is proposed to measure the Single Spin Asymmetries of the Semi-Inclusive Deep Inelastic Scattering (SIDIS) process  $\vec{n}(e, e'\pi^\pm(K^\pm))$ , using the large-solid-angle Super Bigbite Spectrometer (SBS), the BigBite Spectrometer, and a novel polarized  $^3\text{He}$  target that includes alkali-hybrid optical pumping and convection flow to achieve very high luminosity. Both spectrometer arms will utilize GEM-based tracking to accommodate the high rates. The abundant statistics will allow the determination of the Collins and Sivers functions for neutron roughly 10 times more accurate than obtained for proton at HERMES for a detailed grid of the kinematic variables  $x$ ,  $p_T$ , and  $z$ . Furthermore, by including data taking at two energies, an 8.8 and 11 GeV, we will have data at two values of  $Q^2$  for each bin in  $x$ .

The azimuthal coverage of our experiment is excellent, and is facilitated by collecting data at a series of neutron polarization directions, always transverse to the beam direction. The SIDIS pions and kaons will be detected over a wide range of the hadron momenta above 2 GeV for the angle between the hadron production and the electron scattering planes up to  $\pm 60^\circ$ , and the angle between the hadron momenta and the virtual photon momenta up to  $60^\circ$ . Between the large acceptances of the electron and hadron arms, an electron polarized-nucleon luminosity on the level of  $4 \cdot 10^{36} \text{ cm}^{-2}/\text{s}$ , and a target polarization of 65%, we will obtain in a two-month run about 100 times more statistics (after accounting for difference in polarization and dilutions) than was done by the HERMES experiment. The experiment has significant potential for the discovery of new effects in hadron physics.

# Chapter 1

## Partonic Structure of the Nucleon

There are a large number of review articles which thoroughly document the status of the field, see e.g. [1]; in this section we provide a general overview and some details concerning aspects of quark transverse degrees of freedom. The discovery and study of the partonic structure of hadrons present a great success story of particle physics. Experiments have obtained significant insights into QCD without the use of quark beams. Quark distributions and quark polarizations have been probed by virtual photons over a wide range of the momenta.

In the case of inclusive electron scattering ( $e, e'$ ) there is a kinematic difference between studies of nuclei and studies of the nucleon due to difference in the ratio of the relevant constituent mass,  $m$ , and binding energy,  $U$ . In nuclei, with a constituent nucleon of 1 GeV mass and binding energy of 10 MeV, this ratio is 100 but in a nucleon, whose constituent is a quark of few MeV mass with a binding energy of a few hundreds MeV, the ratio is 0.01. This large difference in the  $m/U$  ratio necessitates a change from the non-relativistic shell model of the nuclei to the parton model of the nucleon described in the infinite momentum frame and explains the success of the collinear approximation for the leading twists QCD diagrams. There are also fundamental differences between nucleon-nucleon forces and parton interactions within the nucleon, the foremost being the realization of quark confinement.

Using the semi-inclusive process of nucleon knockout from nuclei, ( $e, e'p(n)$ ), experiments provide insight into nucleon momentum distributions, final-state interactions, and subtle effects associated with nucleon binding; high quality studies of nucleon knockout from the nuclei have proved productive. However, experiments utilizing beams of free nucleons are the primary source of information on the nucleon-nuclei interaction. In the same manner, the semi-inclusive process from a nucleon can provide unique information at the nucleon level. The electro-production of hadrons from nucleons involves the fragmentation of the struck quark and its interaction with the remnant nucleon. In spite of these complications, the key features of the struck quark characteristics can be investigated. Semi-inclusive deep inelastic scattering, SIDIS, provides access to the quark transverse momentum dependent distributions (TMDs), some of which result from the spin of the nucleon. The study of SIDIS contributes to our understanding of the origin of quark orbital angular momentum and flavor decomposition of PDFs.

The proposed experiment will study reaction  $\vec{n}(\vec{e}, e'\pi^\pm(K^\pm))$ , focusing on the measure-

ment of the azimuthal asymmetry of pion and kaon yields with respect to the virtual photon momentum and the direction of nucleon polarization. The experimental setup is optimized for a measurement with the direction of nucleon polarization orthogonal to the electron scattering plane and the transverse moment of the hadron below 0.7 GeV.

In this chapter the basic formalism of the deep inelastic scattering (DIS) and the semi-inclusive DIS are presented.

## 1.1 Deep Inelastic Scattering

In Deep Inelastic Scattering (DIS), a photon exchange is used to probe the structure of the nucleon. The plot in Fig. 1.1 is a representation of the DIS process and introduces kinematic quantities which are defined in Table 1.1. The deep inelastic electron scattering process

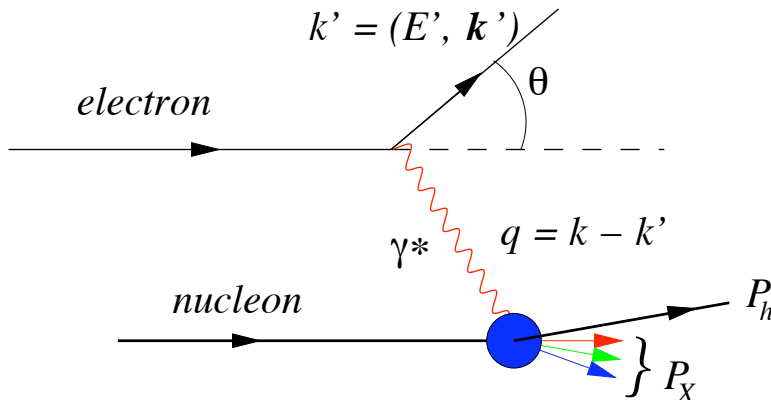


Figure 1.1: Kinematics quantities for description of electron-nucleon scattering:  $k$  and  $k'$  are the four-momenta of incoming and outgoing electrons.

is:  $e(k) + N(P) \rightarrow e'(k') + X(P_X)$ . The initial electron ( $e$ ) with 4-momentum  $k = (E, \mathbf{k})$  exchanges a photon of 4-momentum  $q$  with a target ( $N$ ) with 4-momentum  $P$ . In an inclusive process experiment the outgoing electron ( $e'$ ) with 4-momentum  $k' = (E', \mathbf{k}')$  is detected. The DIS process is often modeled in the Bjorken limit in which  $Q^2$  and photon energy  $\nu$  both go to infinity while the ratio,  $x_{Bj} = Q^2/(2M\nu)$ , is held fixed. Another useful dimensionless variable is  $y = \nu/E$ , the fractional energy loss of the electron in the scattering process. The target's spin 4-vector  $\mathbf{S}$  describes the target polarization direction in the lab frame. This direction,  $\mathbf{S}$ , is often decomposed into  $S_L$  and the  $\mathbf{S}_T$ , longitudinal and transverse projections with respect to the direction of the 3-momentum of the virtual photon.

Three parton distribution functions describe the structure of the nucleon at leading twist: the unpolarized distribution  $f_1(x)$ , the helicity distribution  $g_1(x)$ , and the transversity distribution  $h_1(x)$ . The function  $f_1(x)$  is the quark density in the an unpolarized nucleon. The function  $g_1(x)$  presents the distribution of longitudinally polarized quarks in a longitudinally polarized nucleon (with respect to the  $\gamma^*$  3-momentum). The transversity distribution,  $h_1(x)$ , describes the distribution of transversely polarized quarks in a nucleon transversely polarized with respect to the  $\gamma^*$  3-momenta. The Figure 1.2 shows a schematic representation for the

$M$		Mass of target nucleon
$k$	$= (E, \mathbf{k})$	4-momenta of the initial state electron
$P$	$\stackrel{lab}{=} (M, 0)$	4-momentum of the initial target nucleon
$S_T$		Target's spin 4-vector
$k'$	$= (E', \mathbf{k}')$	4-momenta of the final state electron
$\theta$		Polar angle of the scattered electron
$q$	$= (E - E', \mathbf{k} - \mathbf{k}')$	$\gamma^*$ 4-momentum
$Q^2$	$= -q^2$	Negative squared 4-momentum transfer
$\nu$	$= P \cdot q / M$	$\gamma^*$ energy in the target rest frame
$\epsilon$	$\stackrel{lab}{=} \left[ 1 + 2 \frac{\nu^2 + Q^2}{Q^2} \tan^2 \frac{\theta_e}{2} \right]^{-1}$	$\gamma^*$ polarization parameter
$y$	$= (P \cdot q) / (P \cdot k) \stackrel{lab}{=} \nu / E$	$\gamma^*$ fractional energy
$x$	$= Q^2 / (2P \cdot q) \stackrel{lab}{=} Q^2 / (2M\nu)$	Bjorken scaling variable $x$
$s$	$= (k + P)^2 = Q^2 / xy + M^2$	Square of the total 4-momentum
$z$	$= E_h / \nu$	Elasticity, fractional energy of the observed hadron
$W^2$	$= (P + q)^2 =$ $= M^2 + 2M\nu - Q^2$	Squared invariant mass of the $\gamma^*$ -nucleon system
$P_h$	$= (E_h, \mathbf{P}_h)$	4-momentum of an observed hadron
$P_\perp$		Component of $\mathbf{P}_h$ perpendicular to $\mathbf{q}$
$\phi$		Angle between the scattering and hadron production planes
$\phi_S$		Azimuth of the nucleon spin with respect to $\mathbf{q}$
$W'^2$	$= (M + \nu - E_h)^2 -  \mathbf{q} - \mathbf{P}_h ^2$	invariant mass of the hadron system

Table 1.1: Kinematic variables of DIS and SIDIS (the definition of azimuthal angles follow the Trento convention [36]).

leading parton distributions.

### Inclusive DIS Cross Sections

The differential cross section of inclusive inelastic  $eN$  scattering process is written in the usual notation as:

$$\frac{d^2\sigma}{dE'd\Omega_{e'}} = \frac{\alpha^2}{4E^2 \sin^4(\frac{\theta}{2})} \left[ W_2(q^2, \nu) \cos^2(\frac{\theta}{2}) + 2W_1(q^2, \nu) \sin^2(\frac{\theta}{2}) \right].$$

In the approximation of  $E, E' \gg M$  and finite  $q^2, \nu$  we will use

$$\frac{d^2\sigma}{dE'd\Omega_{e'}} \approx \frac{\alpha^2}{4E^2 \sin^4(\frac{\theta}{2})} \frac{F_2(q^2, \nu)}{\nu}.$$

It also could be written as:

$$\frac{d^2\sigma}{dx dy} = \frac{4\pi\alpha^2(s-M^2)}{Q^4} \left[ (1-y)F_2 + y^2 x F_1 - \frac{M^2}{(s-M^2)} xy F_2 \right]$$

where  $F_1, F_2$  are DIS structure functions.

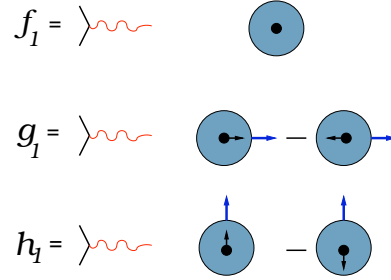


Figure 1.2: Schematic notations for SIDIS, transverse momentum independent structure functions.

The differential cross section for the electro-production of a hadron,  $h$ , for unpolarized beam and unpolarized target can be presented as:

$$\frac{d^3\sigma}{dE'd\Omega_{e'}d\Omega_h} = \Gamma \frac{d\sigma_{\gamma^*,h}}{d\Omega_h},$$

where  $\Gamma$  is the virtual photon flux factor, given by:

$$\Gamma = \frac{\alpha}{2\pi^2} \frac{E'}{E} \frac{s-M^2}{2MQ^2} \frac{1}{1-\epsilon},$$

and  $d\sigma_{\gamma^*,h}/d\Omega_h$  is the cross section for hadron production by the virtual photon.

### Semi-Inclusive DIS Cross Sections

The SIDIS cross section for a polarized beam and a polarized target requires six terms schematically written as:

$$\sigma_{\gamma^*,h}(\phi, \phi_S) = \sigma_{UU} + P_e \sigma_{LU}(\phi) + S_L \sigma_{UL}(\phi) + P_e S_L \sigma_{LL}(\phi) + S_T \sigma_{UT}(\phi, \phi_S) + P_e S_T \sigma_{LT}(\phi, \phi_S),$$

where  $P_e$  is the polarization of the beam while  $S_T$  and  $S_L$  describe the transverse and longitudinal polarization of the target.

There are three types of twist-2 transverse momentum independent quark distributions for the nucleon. These are:

1. the spin-independent distributions  $q(x)$  for each flavor measured in the unpolarized structure functions  $F_1$  and  $F_2$ ,
2. the spin-dependent distributions  $\Delta q(x)$  measured in  $g_1$  and
3. the transversity distributions  $\delta q(x)$ .

As soon as the transverse momentum of the parton relative to the nucleon is taken into account, at the leading order, 5 additional distribution functions for a total of 8 Transverse Momentum Dependent (TMD) functions (see fig. 1.3) enter into the description of the nucleon; two of them, Sivers and the Pretzelocity will be introduced later in this chapter.

In the parton model the DIS structure functions  $F_1$  and  $F_2$  are written as:

		quark		
		U	L	T
nucleon	U	q 		$h_{1U}^\perp$  - 
	L		$\Delta q$  - 	$h_{1L}^\perp$  - 
	T	$f_{1T}^\perp$  - 	$g_{1T}^\perp$  - 	$\delta q$  -  $h_{1T}^\perp$  - 

Figure 1.3: Pictorial view of the Transverse Momentum Dependent quark distribution functions, describing the nucleon at the leading twist.

$$F_1(x) = \frac{1}{2x} F_2(x) = \frac{1}{2} \sum_q e_q^2 \{q + \bar{q}\}(x)$$

here the  $\{q + \bar{q}\}(x) = (q^\uparrow - \bar{q}^\uparrow)(x) + (q^\downarrow - \bar{q}^\downarrow)(x)$

The polarized structure function,  $g_1 = \sigma_{LL}/\sigma_{UU}$ , is written as:

$$g_1(x) = \frac{1}{2} \sum_q e_q^2 \Delta q(x)$$

where  $\Delta q(x) = (q^\uparrow - \bar{q}^\uparrow)(x) - (q^\downarrow - \bar{q}^\downarrow)(x)$ .

The transversity distributions,  $\delta q(x)$ , describe the density of transversely polarized quarks inside a transversely polarized proton.

$$\delta q(x) = q^\uparrow(x) - q^\downarrow(x)$$

## 1.2 Transversity

Now we focus on the transversity physics and SIDIS cross section term  $\sigma_{UT}$ . This term involves a transversely polarized target and an unpolarized beam and introduces an azimuthal-dependent cross section. Using variables defined in Table 1.1, this cross section can be written as:

$$\frac{d\sigma_{\gamma^*,h}}{dx dy dz d\phi_h} = d\sigma_{UU} + |S_T| d\sigma_{UT}(\phi, \phi_S) \quad (1.1)$$

The cross section for the unpolarized beam and the unpolarized target could be presented as<sup>1</sup>:

<sup>1</sup>At the leading twist 2 an additional  $\cos 2\phi$  term is present, and will be considered in the analysis section.

$$d\sigma_{UV} = \frac{4\pi\alpha^2 s}{Q^4} (1 - y - \frac{y^2}{2}) \sum_q e_q^2 [f_1^q \otimes D_1^q] \quad (1.2)$$

The  $\sigma_{UT}$ , at the leading twist-2 order can be decomposed into the Collins, Sivers and Pretzelosity terms [29]:

$$d\sigma_{UT}^{Collins} = \frac{4\pi\alpha^2 s}{Q^4} (1 - y) \sin(\phi + \phi_s) \sum_q e_q^2 [w_C \cdot h_1^q \otimes H_1^{\perp q}] \quad (1.3)$$

$$d\sigma_{UT}^{Sivers} = \frac{4\pi\alpha^2 s}{Q^4} (1 - y - \frac{y^2}{2}) \sin(\phi - \phi_s) \sum_q e_q^2 [w_S \cdot f_{1T}^{\perp q} \otimes D_1^q] \quad (1.4)$$

$$d\sigma_{UT}^{Pretzelosity} = \frac{4\pi\alpha^2 s}{Q^4} (1 - y) \sin(3\phi - \phi_s) \sum_q e_q^2 [w_P \cdot h_{1T}^q \otimes H_1^{\perp q}] \quad (1.5)$$

where the convolution on the right hand side involve the integral on the initial ( $\mathbf{k}_T$ ) and final ( $\mathbf{p}_T$ ) transverse momenta of the parton with the corresponding weighting factors  $w_{C,S,P}^2$ :

$$[w_j f \otimes H] = x \int d^2 \mathbf{p}_T d^2 \mathbf{k}_T \delta^{(2)}(\mathbf{p}_T - P_{\perp}/z - \mathbf{k}_T) \cdot w_j(\mathbf{P}_{\perp}, \mathbf{k}_T, \mathbf{p}_T) \cdot f(x, \mathbf{k}_T, Q^2) \cdot H(z, \mathbf{p}_T, Q^2)$$

where  $f$  and  $H$  are respectively a TMD function and a fragmentation function, and in particular:

$h_1^q$  is the Transversity TMD, directly related to the above defined transversity, by an integration in  $\mathbf{P}_{\perp}$

$f_{1T}^{\perp q}$  is the Sivers function, related to the correlation between parton spin and orbital angular momentum (zero orbital angular momentum implies a vanishing Sivers function). Its non zero value also imply a final state interaction.

$h_{1T}^q$  is the Pretzelosity function [37], related to the interference of orbital angular momentum wave functions differing by 2 units. This term is suppressed by a mass factor presents in  $w_P$ .

$H_1^{\perp q}$  is the Collins fragmentation function, which correlates transversely polarized parton with unpolarized final hadron

$D_1^q$  is the relatively well know and measured unpolarized fragmentation function.

In the following discussion we will omit the Pretzelosity term for simplification of notation; however it is our intention to include it in the extraction of the other function, as discussed in section 5.6.

---

<sup>2</sup>The weight  $w$  is function of combination of scalar products of the transverse momenta of the parton and final hadron.

From the cross sections, we can construct the single spin asymmetry, **SSA**, written as:

$$A_{UT} \equiv \frac{1}{|S_T|} \frac{d\sigma(\phi_h, \phi_s) - d\sigma(\phi_h, \phi_s + \pi)}{d\sigma(\phi_h, \phi_s) + d\sigma(\phi_h, \phi_s + \pi)} = \frac{1}{|S_T|} \frac{d\sigma_{UT}}{d\sigma_{UU}} \quad (1.6)$$

being  $d\sigma_{UT}(\phi_s + \pi) = -d\sigma_{UT}(\phi_s)$ .

This full SSA, in first approximation, contains the Collins and the Sivers parts modulated by the sin function of different combinations of the azimuthal angles.

$$A_{UT} = A_{UT}^{Collins} \sin(\phi + \phi_s) + A_{UT}^{Sivers} \sin(\phi - \phi_s) \quad (1.7)$$

where the Collins and Sivers asymmetries are related to the above distribution and fragmentation function by corresponding (first order) moments:

$$A_{UT}^{Collins} = 2 \frac{\int d\phi_S d^2\mathbf{P}_\perp \sin(\phi + \phi_s) d\sigma_{UT}}{\int d\phi_S d^2\mathbf{P}_\perp d\sigma_{UU}}$$

and

$$A_{UT}^{Sivers} = 2 \frac{\int d\phi_S d^2\mathbf{P}_\perp \sin(\phi - \phi_s) d\sigma_{UT}}{\int d\phi_S d^2\mathbf{P}_\perp d\sigma_{UU}}$$

where the integration in  $\mathbf{P}_\perp$  requires a specific prescription (assumption), for example in the form of dependence of the distribution and fragmentation functions from the corresponding quark transverse momenta (such as the Gaussian ansatz used in 5).

The Collins [2, 3] and Sivers [4] asymmetries have very different origin and reveal new features of the nucleon structure.

### 1.3 Spin-orbit effects and the FSI in nuclear physics

In a non-relativistic model of an atom, the spin-orbit (LS) term of the Hamiltonian appears due to the electron's magnetic moment. This LS term is responsible for many phenomena, including the fine splitting in atomic level structure which allows high polarization of the CEBAF beam and also the Mott-based polarimetry used for the CEBAF beam. In the low-energy nucleon-nucleon and nucleon-nuclei interaction the role of spin-orbit interactions is even more pronounced; JLab experiments use it to determine the proton polarization at the level of accuracy required for the measurement of the electric form factor of proton.

The importance of spin-orbit effects in hadron physics was discovered many years ago. However, such effects obviously require quark transverse momentum, which was excluded by the collinear approximation, and was neglected for some time. The EMC discovery of the "spin crisis" brought attention to the issue of parton orbital angular momentum and transverse spin physics. In absence of a free quark beam, the SIDIS process provides a good substitute since the parameters of a struck quark, after absorption of the virtual photon, can be calculated.

## 1.4 Transverse momentum physics and an impact parameter at large $Q^2$

M. Burkardt has presented the phenomenology and applications of the impact parameter representation of the Generalized Parton Distributions to the SIDIS process in a number of articles [5, 6]. The impact parameter is defined as a distance from the point of interaction

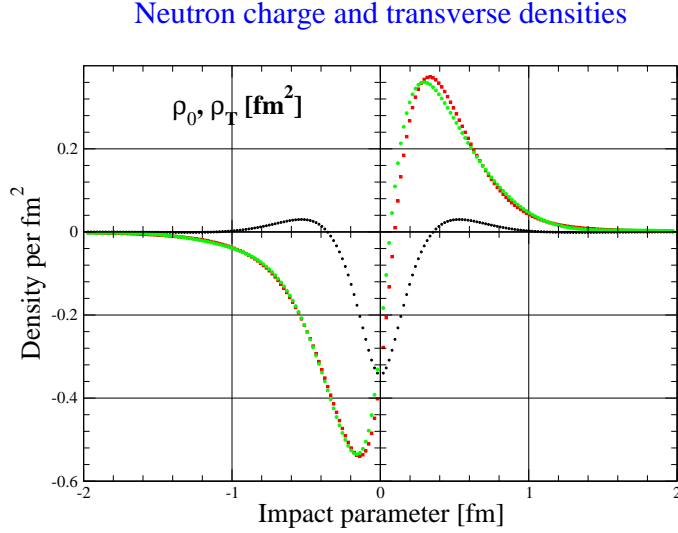


Figure 1.4: Charge density (black) and transverse density of the neutron.

of the virtual photon with the struck quark to the transverse center of the longitudinal momentum, which in turn is defined by  $\mathbf{r}_\perp = \sum_q x_q \cdot \mathbf{r}_{\perp,q}$  where the sum is over all quarks.

When a virtual photon is absorbed by a transversely polarized nucleon the quark density has some azimuthal variation [5]. The amplitude of such variation is directly related to the experimentally observed form factors of the elastic electron scattering from nucleon. This was calculated first in [7, 8] (see Fig. 1.4). The connection between densities the impact-parameter dependent densities and the form factors follow from the results:

$$q(x, \mathbf{b}_\perp) = \int \frac{d^2q}{(2\pi)^2} e^{i \mathbf{q} \cdot \mathbf{b}_\perp} H_q(x, t = -\mathbf{q}^2)$$

$$\rho_0(b_\perp) \equiv \sum_q e_q \int dx q(x, \mathbf{b}_\perp) = \int d^2q F_1(\mathbf{q}^2) e^{i \mathbf{q} \cdot \mathbf{b}_\perp}$$

$$\rho_0(b_\perp) = \int_0^\infty \frac{Q \cdot dQ}{2\pi} J_0(Qb_\perp) F_1(Q^2)$$

$$\rho_T(\mathbf{b}_\perp) = \rho_0(b_\perp) - \sin(\phi_b - \phi_s) \int_0^\infty \frac{dQ}{2\pi} \frac{Q^2}{2M} J_1(Qb_\perp) F_2(Q^2)$$

As suggested by M. Burkardt, in the process of struck-quark fragmentation the leading hadron obtains an azimuthal anisotropy due to attraction from the nucleon remnant. Such final state interactions correspond to the Sivers effect. Deformation of the quark distribution in a polarized nucleon also results in an orbital angular momentum of the quarks and is related to the quark anomalous magnetic moment. The effect of a flavor segregation naturally leads to the different sign of SSA for the positive and negative pions, which is in agreement with recent HERMES results [9].

## 1.5 Experimental and theoretical status

The first measurements of the Collins and Sivers asymmetries have been performed recently by the HERMES on proton [40] and COMPASS on deuteron [38] and very recently on proton [39].

The two experiments overlap in the  $x$  range (upper central value limit is  $\sim 0.3$ ) but cover quite different  $Q^2$  kinematics regions ( $Q_{HERMES}^2$  up to  $\sim 10$  GeV<sup>2</sup>,  $Q_{COMPASS}^2$  up to  $\sim 100$  GeV<sup>2</sup>) and therefore direct comparison of their data requires careful analysis which are probably not fully under control yet.

In fact, the results from the two experiments clearly show:

- direct measurements exist for proton and deuteron targets only, with limited statistics for kaon.
- a non zero Collins asymmetry in the proton (both HERMES and COMPASS)
- a non zero Sivers asymmetry seen in HERMES but not in COMPASS
- compatible with 0 deuteron asymmetries (COMPASS)
- a significant  $K^+$  Sivers asymmetry (even larger than  $\pi^+$ , (HERMES))
- evident and surprising Sivers flavor dependence (HERMES)

Direct data on neutron is under measurement in Hall A (experiment E06-010 [35]) and it is expected to cover the  $x$  region between 0.1 and 0.4 at a  $Q^2$  similar to HERMES, with a statistical accuracy compared to the existing experiments; this will be the only available data on neutron in the coming years.

The latest analysis from HERMES, presented at SPIN08 [33] for the Collins and Sivers respectively), has for the first time succeeded to extract the two asymmetries on 2 dimensional grids of the three combinations of the relevant variables  $x$ ,  $z$  and  $P_\perp$  (reported in figures 1.5 and 1.6 the  $(x, z)$  results).

Intense and quite extended program on the Transverse Momentum Dependent distribution functions is carried on by the CLASS collaboration (which already measured a non-zero

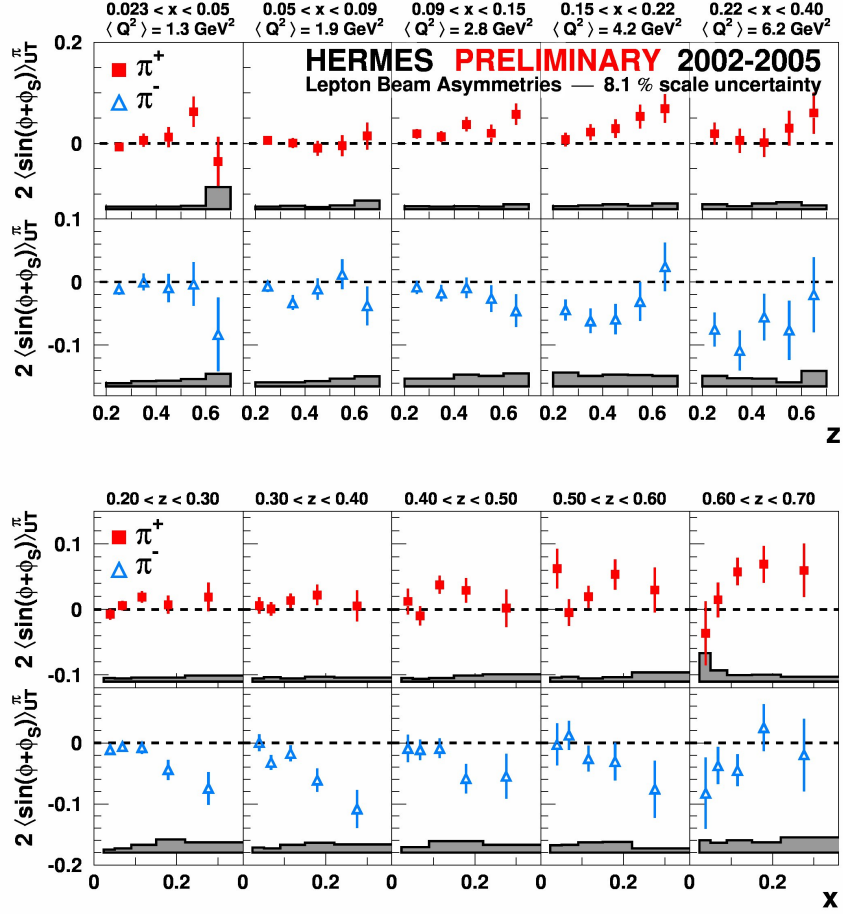


Figure 1.5: The first (and unique) 2D grid proton Collins moments extracted by HERMES and presented in [33].

beam-spin azimuthal asymmetry coming from higher twists terms) and will be further expanded in the CLASS12 era, possibly with a HD transversely polarized target [41] whose compatibility with a relatively high intensity electron beam shall be proven.

The above results from HERMES and COMPASS have stimulated and motivated intense theoretical studies on the spin nucleon structure which have originated new conceptual frameworks such as the Generalized Parton Distribution functions.

Very recently Anselmino and collaborators have extracted, for the first time, the Transversity and Collins functions for the valence  $u$  and  $d$  quarks, based on a global analysis (fit) of the HERMES proton data, COMPASS deuteron results and BELLE  $e^+e^-$  data [42].

Moreover the same group also extracted a new parameterization of the Sivers function presented in [43].

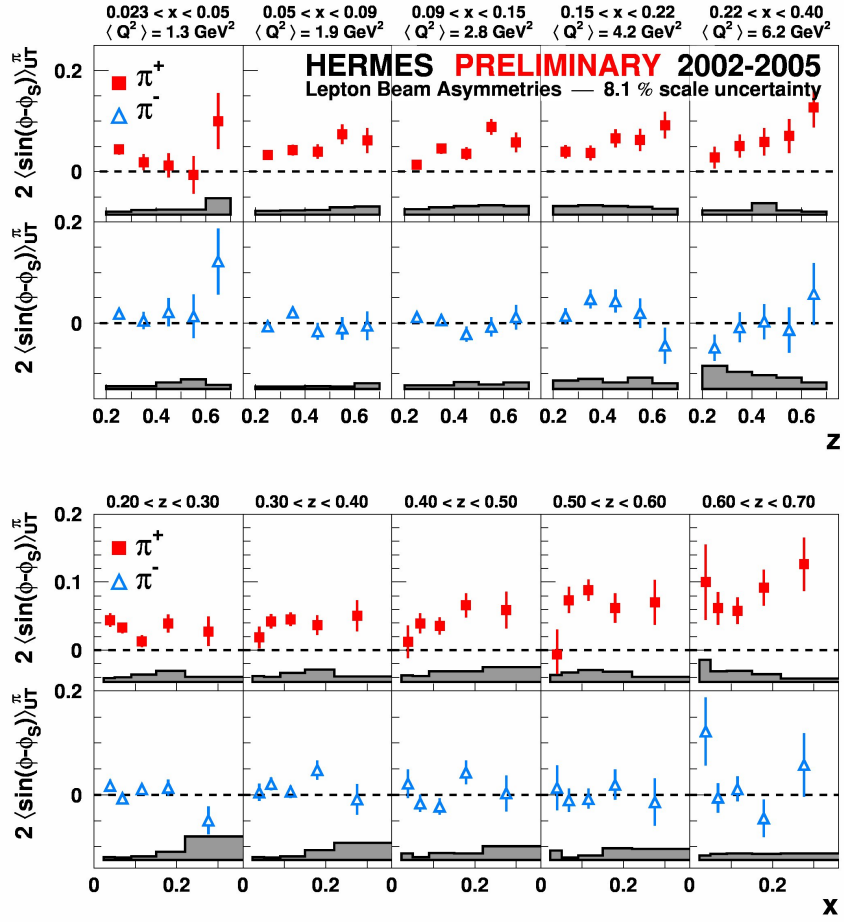


Figure 1.6: The first (and unique) 2D grid proton Sivers moments extracted by HERMES and presented in [33].

## Chapter 2

# Proposed Measurements

### 2.1 Overview

This section starts from a concept of SIDIS experiments, moves through the proposed detector configuration, and formulates the main elements of the experiment run plan. A study of the novel features of QCD dynamics in a nucleon is possible via Semi-Inclusive Deep Inelastic Scattering, which has been investigated with high accuracy by HERMES and COMPASS experiments [9, 10]. Nevertheless, there remain very interesting questions which require a polarized target for investigation and much larger statistics than presently obtained. These include TMD distributions and the related functions  $h_{\perp}, H_{\perp}$ , which are accessible only with the transversely polarized target.

The spin observables allow evaluations of the spin and orbital angular momenta of the nucleon constituents and provide powerful tests of nucleon models. Since the EMC experiment at CERN, a large body of data on the polarization observables have been accumulated. The significant role of quark orbital angular momentum has been established. The phenomenology of semi-inclusive processes, including models of GPDs and TMDs, are the central issues of hadron physics today. The statistical and systematic accuracy which can be achieved by these measurements open the possibilities for decisive tests of theory and future discoveries in this field.

The upgrade of the CEBAF accelerator to 11 GeV opens a tremendous opportunity for study of SIDIS processes because, in addition to the beam quality, it will provide the range of kinematics needed for a unique SIDIS program. The SIDIS experiments, in most important cases, require just a two-arm experimental setup with an electron arm and a hadron arm. The electron arm is used to tag the deep-inelastic events and determine the virtual-photon 4-momentum. The hadron arm apparatus is used to detect the leading hadron, which takes most of virtual photon momentum. The use of a polarized target will allow access to the spin-observables, including measurements of single-spin asymmetries (SSA). Optimization of a SSA measurement must provide sufficient statistics and maximum coverage range in each of four variables: the Bjorken  $x$ , the hadron energy  $z$ , the hadron transverse momentum  $p_t$ , and the momentum transfer  $Q^2$ . For measurement of the azimuthal variations, wide coverage is needed for both  $\phi$  (the angle between hadron production plane and the electron scattering plane) and  $\phi_s$  (the angle between target polarization and the electron scattering plane).

Wide  $\phi$  and  $\phi_s$  coverage could be achieved, for example, by the use of several directions of the target polarization. In fact, a large out-of-plane acceptance of the both arms allows complete coverage with just two polarization directions - vertical and horizontal. For an experiment utilizing the 11 GeV beam, the pion and kaon momentum would be between 2 and 5 GeV for  $z$  above 0.5 so the angular acceptance of  $12^\circ$  will allow acceptance of particles with  $p_t$  up to 1 GeV.

The design of an optimized experiment is always a compromise between performance, preparation time, and cost. The parameters of the polarized target have significant impact. The polarized  $^3\text{He}$  target offers a luminosity of  $10^{38}$   $\text{cm}^{-2}/\text{s}$ , while the low temperature HD target has very good parameters for luminosity around  $10^{34}$   $\text{cm}^{-2}/\text{s}$ , so the two types of targets are suited for different types of the detector configurations: the polarized  $L^3\text{He}$  target is suited to the moderate solid angle setup with excellent PID of  $e/\pi/K$  in full momentum range while the HD target is suited to a detector with very large (nearly  $4\pi$ ) acceptance.

We propose to base the hadron arm on the Super Bigbite Spectrometer [13]. The concept and design of this spectrometer was initiated by the GEP5 experiment [14], which will measure the proton form factors ratio at very large momentum transfer. Basic parameters of the SBS are shown in Tab. 2.1. The acceptance of the SBS will be in the range of

$\theta_{central}$ , degree	$\Omega$ , msr	D, meter	$\Delta\Theta_{hor}$ , degree	$\Delta\Theta_{ver}$ , degree
3.5	5	9.5	$\pm 1.3$	$\pm 3.3$
5.0	12	5.8	$\pm 1.9$	$\pm 4.9$
7.5	30	3.2	$\pm 3$	$\pm 8$
15	72	1.6	$\pm 4.8$	$\pm 12.2$
30	76	1.5	$\pm 4.9$	$\pm 12.5$

Table 2.1: The solid angle of SBS vs. spectrometer central angle. D is the distance from the pivot to the magnet yoke.  $\Delta\Theta_{hor}$  and  $\Delta\Theta_{ver}$  are horizontal and vertical range of the acceptance.

1 to 2 radians in azimuthal angle, and 5 to  $10^\circ$  in polar angle, depending on the central scattering angle,  $\theta_{central}$ . At angles of  $15^\circ$  the solid angle of the SBS allows capture of a significant part of the reaction products from semi-inclusive processes in one setting of the detector. The large solid angle, wide momentum acceptance from 1 GeV and up, resolution of 1%, and the ability to detect particles of both polarities combine to make the SBS a very attractive hadron arm. The compact geometry of this hadron arm make it is easy design an optimized electron arm designed around the existing BigBite spectrometer. Figure 2.1 shows a schematic representation of the angular acceptance the hadron arm and the electron arm.

## 2.2 Physics Goals

We propose to measure the  $\pi^\pm$  and  $K^\pm$  Single-Spin Asymmetries on a transversely polarized nucleon target at series of kinematic settings which correspond to a grid covering the four variables;  $x$ ,  $z$ ,  $p_T$ , and  $Q^2$ , with statistical and systematic accuracy better than 0.5% in each two-dimensional bin. The physics goal is to investigate the nature of the  $A_{UT}$  asymmetries

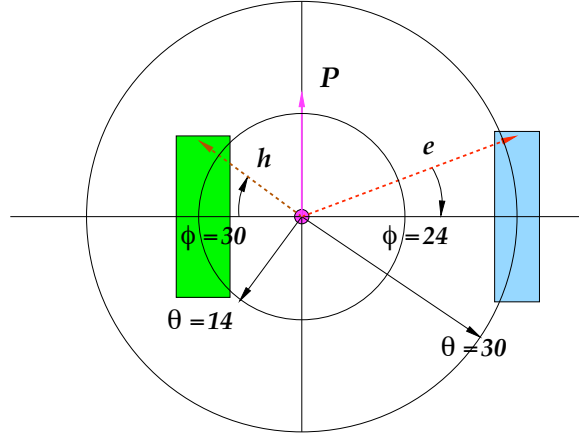


Figure 2.1: The schematic angular acceptance of the setup with SBS and BB viewed along the beam direction. The central angles are:  $\theta_h = 30^\circ$  for BB and  $\theta_e = 14^\circ$  for SBS. Azimuthal ranges in respect to the beam are:  $\pm 24^\circ$  for BB and  $\pm 30^\circ$  for SBS.

by means of precision measurements with minimum assumptions about high-twist role,  $Q^2$  evolutions, factorization function.

## 2.3 Kinematics

The choice of kinematics is driven by a number of considerations, among them the intent to:

- maximize  $W$  - the hadronic system invariant mass,
- maximize  $W'$  - as  $W$ , but without detected hadron, and
- align the hadron spectrometer central angle to the virtual photon.

Optimization of the main parameters determined that the electron arm will be at fixed angle of  $30^\circ$  and the hadron arm at  $14^\circ$ . The distributions of events are presented in Figures of the chapter 5. The kinematic quantities for these points are summarized in Table 2.2.

run #	$E_{beam}$	$\langle x \rangle = 0.2$	$\langle x \rangle = 0.3$	$\langle x \rangle = 0.4$	$\langle x \rangle = 0.5$	$\langle x \rangle = 0.6$
A	8.8	2.9	4.0	5.0	6.0	6.7
B	11	3.8	5.2	6.6	7.9	9.0

Table 2.2: The kinematics of the proposed data points:  $Q^2$  - average values of momentum transfer for three bins of  $x$ .

The proposed grid has 5 by 5 points in  $x$  &  $z$  or re-binned in  $x$  &  $p_t$  with two values of  $Q^2$  for each bin. The rates and expected statistics will be discussed in the Chapter 5.

## 2.4 Systematics

Th small amplitudes of Sivers and Collins asymmetries require the development of methods to suppress systematic uncertainties. Changing the target polarization direction at regular intervals is a standard, but important procedure for reducing systematics. For example, the polarization of the internal target was changed every 60-90 seconds in the HERMES experiment.. Changing the polarization direction for solid  $\text{NH}_3$ ,  $\text{ND}_3$ , HD targets and high pressure  $^3\text{He}$  targets is more complicated and require much more time. For example, the E06-010 experiment uses 20 minute intervals between changes. The new idea of the convection flow  $^3\text{He}$  target, which was proposed and checked recently by our collaboration, allows a novel approach to the spin-direction change. We plan to rotate the direction of the target holding field without change of the field in the polarization pumping cell. The compensation coils will be used to provide stable beam on the target. We expect that spin-direction will be changed every 120 second with a new polarized target approach (see section 4) without any loss of polarization and without significant dead time for transition period.

## Chapter 3

# Experimental Setup

The experiment will be performed in the TJNAF Hall A. An electron beam will pass through a 60 cm long polarized  $^3\text{He}$  target in the scattering chamber. The scattered electrons will be detected in the BigBite spectrometer and the SIDIS pions and kaons will be detected in the SuperBigbite spectrometer.

The total projected luminosity is of  $2 * 10^{37}$  electron-nucleon  $\text{cm}^{-2}/\text{s}$ , which corresponds to about  $4 * 10^{36}$  electron-polarized neutron. Such electron-polarized nucleon luminosity is about 400,000 times higher than the luminosity used in the HERMES experiment and about 3-4 times higher than any previous experiment involving a polarized  $^3\text{He}$  target. There is only one element of the proposed experiment which needs to be added exclusively for this measurement. This element is a Ring Imaging Cherenkov counter in the SBS spectrometer for high quality hadron identification. As presented later, we plan to reuse the HERMES RICH, properly adapted for SBS.

The layout of the proposed experimental set-up is shown in Fig. 3.1. There are two detector arms: the electron arm and the hadron arm. They are located at  $30^\circ$  and  $14^\circ$  degree on the opposite sides of the beam line.

The measurement of the target single-spin asymmetry presents significant challenge for the control of the target and detector stability because of the long time between target polarization changes. We have find a method (see next chapter) to reduce this time to 120 seconds, which is 10 times shorter than was possible before. We plan to use a set of compensation coils located upstream and downstream of the target to null the beam position and direction changes when the direction of the holding field vary.

### 3.1 CEBAF polarized beam

We plan to use a  $40 \mu\text{A}$  beam with 85% polarization. This value of polarization has already been obtained in many JLab experiments. The beam polarization will be measured with the Hall A Møller/Compton polarimeters to make sure that it is maintained at maximum level. The stability of the beam polarization will be continuously monitored by the Compton polarimeter.

The stability of the product of the beam and the target polarizations will also monitored.

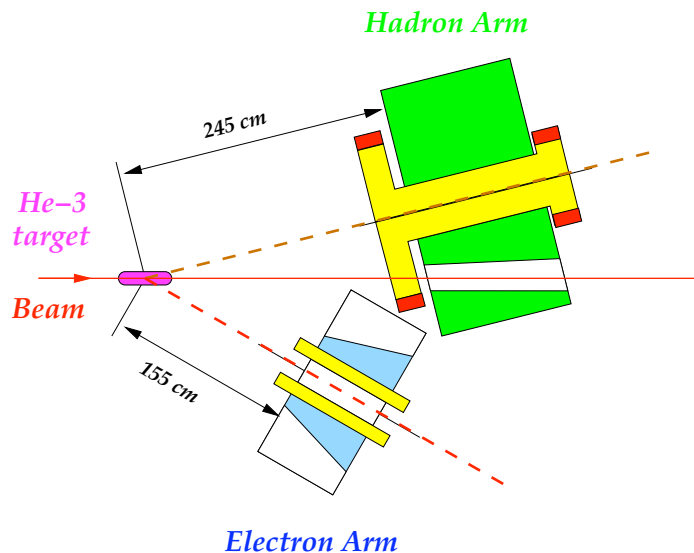


Figure 3.1: The schematic view of the SIDIS two-arm setup.

We plan to do it by using a stand-alone shower calorimeter located in the plane of the target polarization. As it was observed during the GEN1 experiment [11] the counting rate in such a counter has significant helicity dependence due to double spin asymmetry in  $\vec{\gamma}\vec{n} \rightarrow \pi X$  process. The large rate in such a counter allows on-line detection of the possible problem. Because the beam polarization is relatively stable, any change of the double spin asymmetry could indicate to a change in the target polarization.

Additional monitoring of the beam stability will be done by using the HAPPEX system of the beam parameter monitoring and the Lumi monitors, which are located at small angle with respect to the beam line down stream of the target ( $1.5^\circ$ ). The scalers, gated by the signals according to the beam helicity and the target polarization directions, will be used for the beam charge measurement, the triggers rates, and the counting rates of selected individual detectors.

## 3.2 Super Bigbite Spectrometer

The spectrometer was conceived as a part of an approved experiment, E12-07-109, which will measure the proton form factor ratio at momentum transfers up to  $15 \text{ GeV}^2$ . The spectrometer, SBS, in this experiment consists of a dipole, a high resolution tracker, a Ring Imaging Cherenkov counter, and a segmented calorimeter as a trigger. The important feature of SBS, which could be placed at forward angles from  $3.5^\circ$ , is a beam path through the hole in the right yoke of the magnet. Such a configuration is known in the field of accelerator design as a Lamberson magnet, often used for the vertical injection. Figure 3.2 presents a concept of the beam line arrangement and resulting field on the beam line. Another important

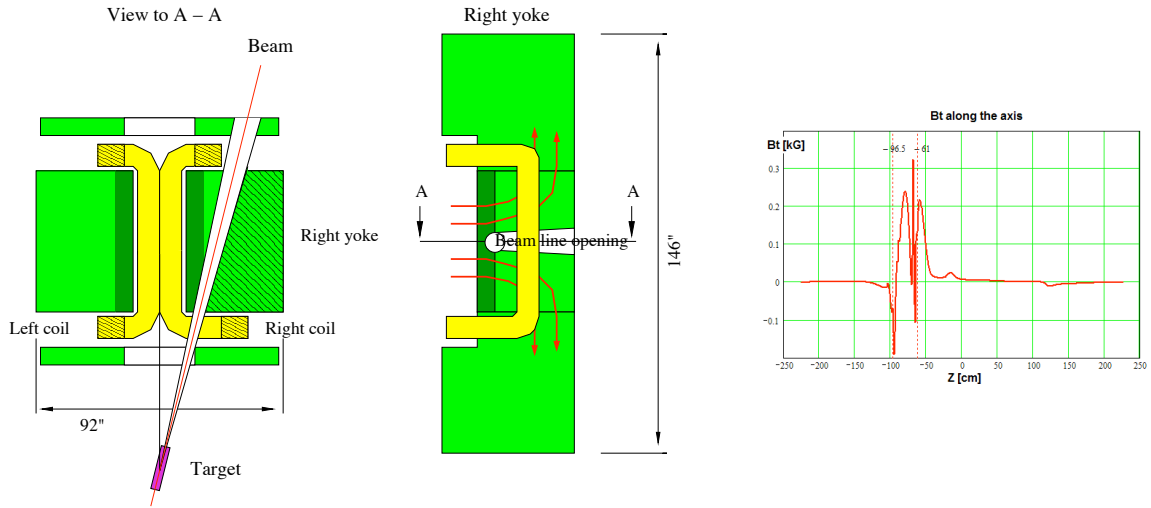


Figure 3.2: The concept of the beam path through 48D48 dipole.

feature of SBS is a high resolution tracker with a high rate capability based on Gas Electron Multiplier detectors invented by F. Sauli [16]. The E12-07-1009, GEP5, experiment will require construction of three trackers. The first tracker, FT, for the momentum analysis of the recoil proton, the second tracker, ST, and the third one, TT, for two polarimeters (needed for the GEP5 experiment). The FT tracker has an area of 40 cm x 100 cm and consists of six chambers. The ST tracker has an area of 100 cm x 200 cm and consists of four chambers. Each chamber is built of 40 cm by 50 cm segments.

For the proposed SIDIS experiment, the magnet will be placed at the distance 245 cm from the target to the return yoke, providing a solid angle of 42(53) msr. The magnet inter-

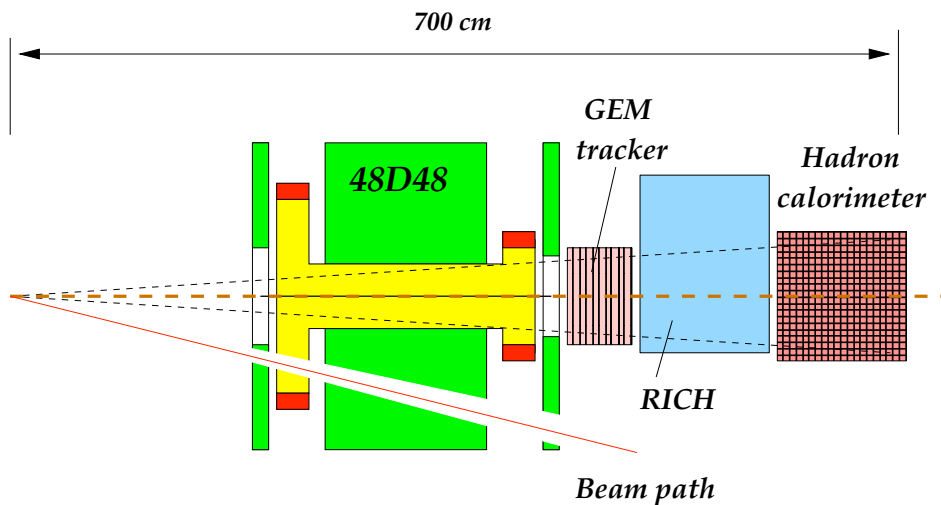


Figure 3.3: The schematic view of the SBS with the detector for the SIDIS experiment.

pole gap has width of 46 cm, so at 14° central angle of SBS the 60 cm long target will be seen

with full solid angle. The magnet is followed by a tracker, a RICH counter, and a hadron calorimeter, HCAL. After the GEP5 experiments, the FT tracker will be reconfigured for use behind the BigBite magnet and ST will be placed closer to the SBS magnet to provide the full 50 cm by 160 cm area coverage with six chambers. The tracker will be followed by a large area RICH counter. Figure 3.3 shows the configuration of SBS for proposed SIDIS experiment.

An additional GEM chamber will be placed behind the RICH mirror. The components of this chamber also will be taken from the Second Tracker of GEP5. The chamber will cover the front face of the hadron calorimeter. The accurate measurement of the coordinates near the calorimeter will allow very simple and reliable data analysis.

Table 3.1 shows the parameters of SBS as it will be used in the proposed experiment. The vertex resolution of SBS is about 0.2 cm, allowing very effective suppression of background from the end-cap windows of the target cell as well as suppression of the accidental events by using the correlation between the vertices reconstructed in the electron arm and in the hadron arm.

Distance from the target to the detector, cm	417
Central angle $\theta_c$ , degree	14
horizontal range: $\Delta\theta_h$ , degree	$\pm 3.6$
vertical range: $\Delta\theta_v$ , degree	$\pm 12$
angular resolution: $\sigma_{\theta_c}$ , degree	0.02
vertex resolution (along beam), cm	0.2
momentum resolution $\sigma_p/p$	$0.001 \times p[\text{GeV}]$

Table 3.1: The parameters of SBS in the SIDIS experiment.

## RICH detector

One key aspect of the proposed experiment will be the extraction of the transverse asymmetry for both pions and kaons; since the population of kaons are expected to be about 1 order of magnitude less than for pions, and of the same order of protons, a good hadron identification system is required (rejection better than 1:100). Such a system will consist of a RICH detector.

The concept of the RICH, the design and even most of the components, are from the dual radiator HERMES experiment<sup>1</sup>, where the counter provided excellent PID over the required momentum range for the pions and the kaons [18].

Fig. 3.4 shows the arrangement of the components in the HERMES RICH counter, while fig. 3.5 presents a schematic view of the working principle of the dual radiator RICH:

- over threshold charged hadrons produce Cherenkov photons in 5 cm thick aerogel wall at the entrance of the detector and possibly along the gas filling the gap between aerogel and mirrors;

<sup>1</sup>One of the two HERMES RICH has been preserved and transported to UVA together with the aerogel wall of the other RICH. All components are in controlled environment at UVA.

- the generated photons are reflected by an array of focusing mirrors<sup>2</sup> on a regular matrix of 3/4" diameter PMTs which sits approximately in the focal surface of the mirrors.
- signal from the PMT is thresholded to provide a binary information which is transferred on 20 MHz serial busses to dedicated buffered VME modules (the total time required for the transfer is  $< 30\mu s$ ).

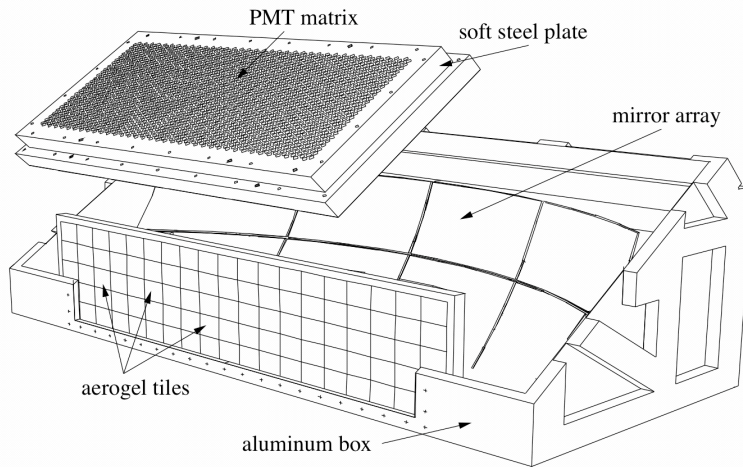


Figure 3.4: The 3D CAD view of the HERMES RICH counter.

The HERMES RICH has an entrance window of  $187 \times 46 \text{ cm}^2$  which fits quite well in the SBS acceptance. The orientation of the RICH longer side will be vertical (as show in figure 3.6, rotated by 90 degree respect to the original horizontal setting in HERMES). The open geometry of SBS allows for the required space for a relatively easy implementation and installation of the RICH.

Fig. 3.7 shows performance of the HERMES counter, which has been very stable during the whole period of operation at HERMES (from 1997 to 2007) [44].

---

<sup>2</sup>Parallel photons coming from the radiators are reflected toward a single point on focal surface.

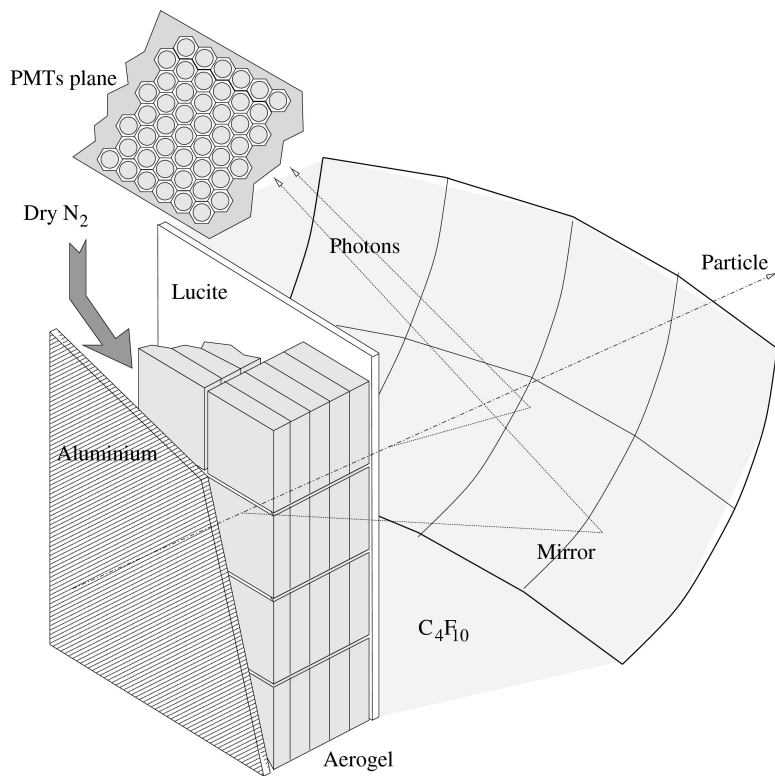


Figure 3.5: The schematic view of the HERMES RICH working principle.

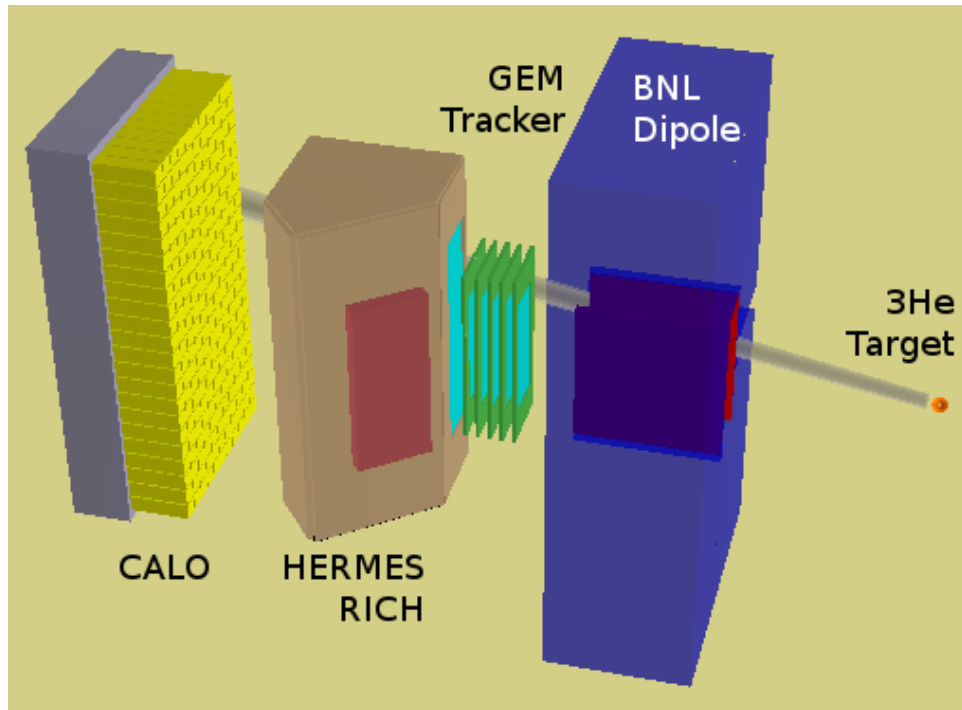


Figure 3.6: Schematic 3D view of the HERMES RICH in the Super BigBite spectrometer.

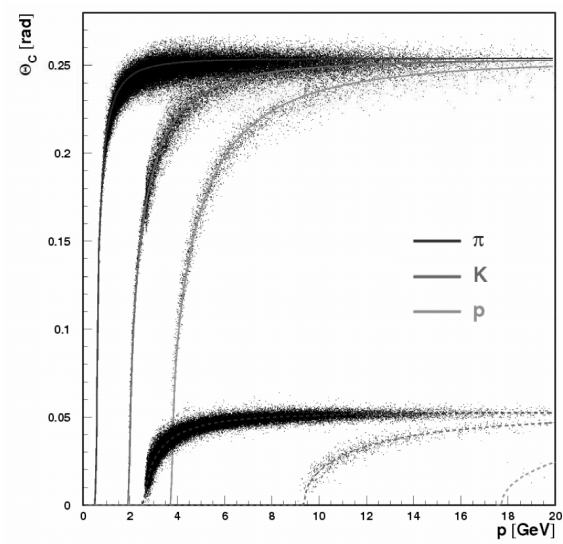


Figure 3.7: PID results from the RICH counter in HERMES.

### 3.2.1 Counting Rates of the Super BigBite Detectors

At the proposed luminosity, the upper limit for the hit rate in the Super BigBite tracker was estimated as 60 kHz/cm<sup>2</sup>. This is three times higher than the 20 kHz/cm<sup>2</sup> obtained from the MC simulation using code developed for the GEP5 experiment with just the <sup>3</sup>He target cell. We used the factor of 3 to allow for differences with the optimized GEP5 setup and possible problems in the optimization of the more complicated polarized target setup. The rate of 60 kHz/cm<sup>2</sup> presents no problem for the GEM operation. The expected hit rate will be about 100 MHz through the whole area of the tracker.

The PID for this experiment requires the use of aerogel in the Cherenkov counter. The aerogel refraction index in the HERMES RICH is 1.03 and the thickness of 5 cm, results in a total weight of 0.67 g/cm<sup>2</sup>. Electrons with energy above 2.1 MeV produce Cherenkov light in this aerogel. The probability of Compton scattering for 2-5 MeV photons in the aerogel is about 3%. The total rate of this background divided by the area of the aerogel was estimated from the flux of photons with energy above 2.1 MeV as 2300 MHz. In the HERMES data the average number of observed photo-electrons per track was 10, so for the electrons produced in the aerogel the corresponding number will be 5. Reduction of the photon yield for electrons near threshold and its distribution accounts for additional reduction of the light yield by a factor of 0.6. Because the electrons kicked by 2-5 MeV photons are moving in a cone with an opening of 0.5 radian or less and the light detection system has 0.83 sr acceptance most of the light will be directed to the PMTs. The resulting rate per PMT will be about 700 kHz. With a 50 ns window time interval relative to the hadron calorimeter time signal, this rate leads to less than a 5% occupancy in the RICH, which is a good operational condition. The dead time of the electronics at this rate could lead to a loss of some of the hits in PMT. It was estimated to be of 7%.

The calorimeter counting rate vs the threshold energy is presented in Fig. 3.8 obtained from the "Wiser" code [19]. The counting rate for the threshold of 2 GeV is about 3 MHz, which means the probability of a second hit in 50 ns time window relative to the electron time signal will be 15%. The corresponding false tracks will be rejected after a check of the correlation of its vertex at the target with the electron arm track vertex at the target.

## 3.3 BigBite Spectrometer

The spectrometer has a 96 msr solid angle when it is used with a short target at a nominal position with 110 cm from the target to the magnet yoke. Figure 3.9 shows the side view of BigBite as it was used during the GEN1 experiment. However, the BigBite magnet will be placed at 30° at distance of 155 cm between the target and the magnet yoke due to geometry constrains. The electron detector package includes a tracker, a Gas Cherenkov counter, a two-layer electromagnetic calorimeter and a scintillator hodoscope. The value of the solid angle for 60 cm long target was found to be of 45 msr.

The BigBite detector package of GEN1 had 15 planes of highly segmented MWDCs, followed by a two-layer lead-glass calorimeter made of 243 blocks of 8.5x8.5x35 cm<sup>3</sup> dimensions and a segmented scintillator hodoscope of 13 two-PMT counters between the two layers of the calorimeter. The "BigFamily" collaboration has upgraded the detector with 3 additional

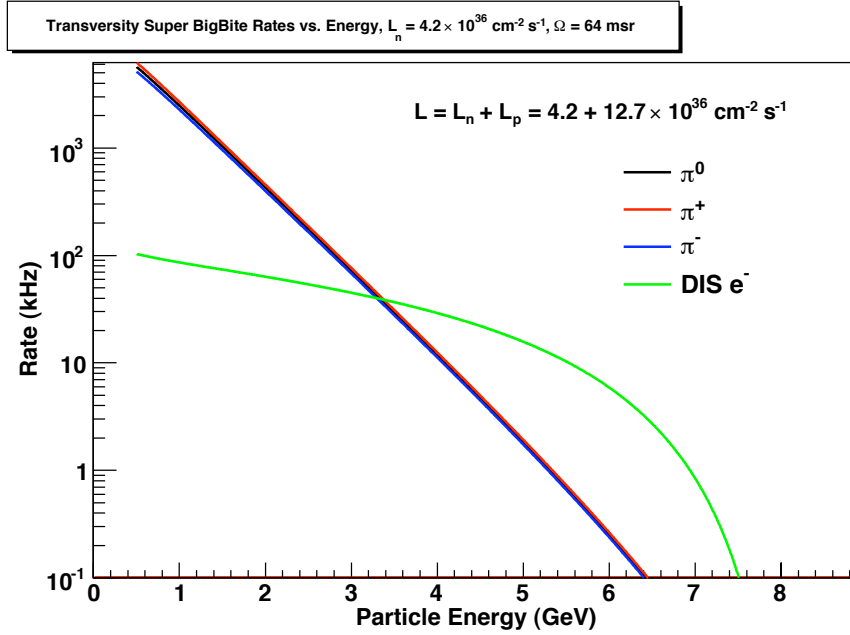


Figure 3.8: The counting rate in the hadron calorimeter of SBS.

MWDC planes and a Gas Cherenkov counter for electron identification. At the luminosity typical for the GEN1 and E06-010 experiments the counting rate in the MWDC is about 20(60) MHz, which is close to the limit for this type detector. For 12 GeV experiments with much higher luminosity, we will replace the MWDCs by the GEM based tracker, which will be assembled from the components of the GEP5 front tracker.

### 3.3.1 Counting Rates of the BigBite Detectors

At projected luminosity, the expected hit rate in the BigBite tracker will be less than 30 kHz/cm<sup>2</sup>. This estimate was obtained by using the observed experimental rate of MWDCs and a MC prediction for the photon flux at higher beam energy. Such a rate is comfortable for the GEM tracker which could operate at rate up to 50 MHz/cm<sup>2</sup>.

The operation of the shower detector is also well understood from our previous experiment with the BigBite spectrometer. The counting rate of the calorimeter expected in the proposed experiment is shown in Fig. 3.10. The threshold level of 1 GeV, which is required in this experiment for lowest  $x$  bin, will result in 200 kHz counting rate. The recently constructed Gas Cherenkov counter will be used for suppression events with non-electron induced trigger rate. Expected rate of the whole Cherenkov counter due to high energy electrons is of 5 kHz. The background counting rate of the Gas Cherenkov counter will be suppressed by using a threshold of 5-6 photo-electrons. Because average number of photo-electrons for good events expected to be about 18 the efficiency of the counter will be above 98% even for the proposed high threshold.

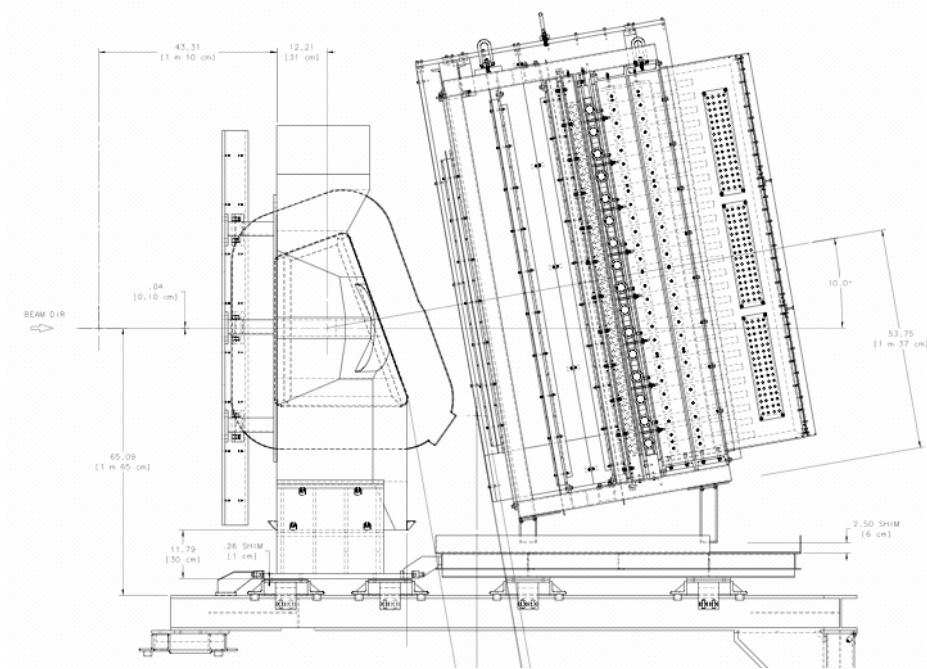


Figure 3.9: The side view of the BigBite spectrometer.

### 3.4 Logic of the Trigger and DAQ rate

The trigger of the hadron arm will use the signal from the hadron calorimeter with 1.5 GeV threshold to insure efficient registration of the hadron with momentum above 2 GeV. The corresponding trigger rate is about 3 MHz, mainly due to hits by the high energy pions. We will use the trigger of the electron arm, which rate is about 5 kHz, as a DAQ trigger without on-line coincidence with the hadron arm. If the actual rate of the electron arm presents problem for DAQ, an additional reduction factor of 6 is possible by requiring a 50 ns coincidence time between the trigger signals of two arms.

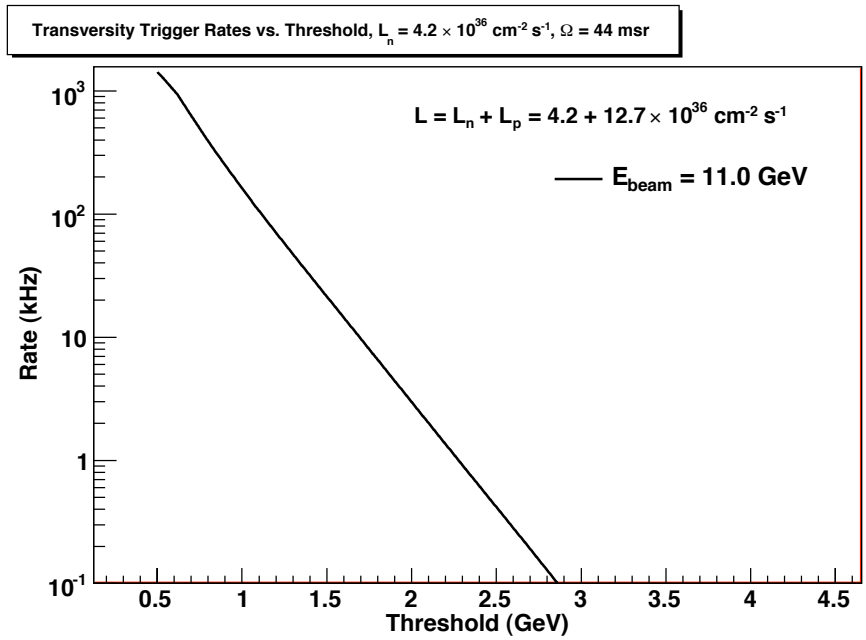


Figure 3.10: The counting rate of the BigBite calorimeter vs threshold.

## Chapter 4

# The Polarized $^3\text{He}$ Target

This section presents the description of the polarized  $^3\text{He}$  target, which is almost identical to the target for the another proposal to PAC34: GEN-II. The direction of the polarization holding magnetic field on the target cell for the present proposal is normal to the beam direction, but in GEN-II should be at  $73^\circ$ , so in GEN-II additional longitudinal field of 7 Gauss will be arranged.

The polarized target for GEN-II will use the technique of spin-exchange optical pumping, the same technique that was used for GEN-I (E02-013), as well as the other polarized  $^3\text{He}$  experiments conducted in Hall A. At first glance, the proposed target for GEN-II appears quite ambitious. The target we describe below will provide an effective luminosity roughly 15-16 times larger than was the case during GEN-I, and 7–8 times larger than the  $^3\text{He}$  experiments that are running at the time of this writing. The fundamental advancements that will provide the improved luminosity, however, have already been largely demonstrated. What distinguishes the GEN-II target from previous polarized  $^3\text{He}$  targets is that it takes better advantage of the progress that has been made in recent years.

There are five distinct factors that play a key role in making the GEN-II target possible:

1. The introduction of alkali-hybrid mixtures to greatly increase the efficiency with which the angular momentum of photons is transferred to  $^3\text{He}$  nuclei.
2. The introduction of greatly improved diagnostics that permit not just polarimetry of the  $^3\text{He}$ , but also polarimetry of the alkali-metal vapors as well as the direct measurement of the alkali-vapor number densities.
3. The advent of commercially available line-narrowed high-power diode-laser arrays.
4. The recognition of the presence of a poorly understood, but measurable,  $^3\text{He}$  spin-relaxation mechanism that can be characterized by something that has come to be called the “X-factor”.
5. The demonstration of convection mixing in sealed target cells with no moving parts.

Of the above mentioned points, only the first, the use of alkali-hybrid mixtures, was employed during GEN-I. By itself, however, this made it possible to maintain a target

polarization of roughly 50% with 8  $\mu$ A of beam on target, considerably better than the range of mid-thirty to low-forty percent polarizations that had been achieved previously. Prior to GEN-I, spin-exchange polarized targets generally used a single alkali metal, rubidium, in the spin-exchange process. When using rubidium, the efficiency with which angular momentum makes its way from circularly polarized photons to  $^3\text{He}$  nuclei is only a few percent. Alkali-hybrid technology involves the use of a mixture of rubidium and potassium. Potassium, it turns out, is much more efficient at transferring its electronic polarization to  $^3\text{He}$  nuclei through spin exchange. When alkali-hybrid mixtures are used, the efficiency with which angular momentum is transferred can be as high as 20–30%. This single advancement made it possible to achieve unprecedented target performance during GEN-I.

The second and third advancements listed above have resulted in improvements to target performance that are at least as significant as those that were achieved by employing alkali-hybrid technology. For the first time, we have begun making target cells that regularly (in the *majority* of those tested) achieve  $^3\text{He}$  polarizations in excess of 70%. Two factors have contributed to this improvement. First, we have optimized the ratio of potassium to rubidium, a process that required more sophisticated target diagnostics. Secondly, we have begun using a new type of commercial line-narrowed high-power diode-laser arrays. Among other things, the new lasers make it possible to maintain alkali-vapor polarizations near 100% even at very high alkali number densities. The polarized  $^3\text{He}$  experiments that are currently running in Hall A are benefitting from these developments. The transversity experiment, for instance, is running with polarizations well in excess of 60% despite the fact that the experiment requires frequent flipping of the  $^3\text{He}$  polarization direction, which causes significant loss of polarization.

The fourth and fifth advancements are of particular relevance to GEN-II. With the implementation of advancements 1–3, the rate at which we can polarize  $^3\text{He}$  nuclei is sufficient to overwhelm rapid depolarization due to the electron beam, even at high beam currents of tens of microamps. As we will show below, however, the basic target-cell design that has been used at JLab in recent years has an intrinsic limitation. The  $^3\text{He}$  is polarized in an upper “pumping chamber”, whereas the electron beam is incident upon the polarized gas in a lower “target chamber”. The connection between these two chambers has historically been accomplished using a single glass tube, referred to as the “transfer tube”. The mixing of gas between these two chambers has been dominated by diffusion, and characterized by time constants on the order of 30–40 minutes. While these mixing times have been quite adequate in the past, we are now able to polarize the gas so quickly that a substantial polarization gradient exists between the pumping chamber and the target chamber. This polarization gradient would be unacceptably large at the currents at which we plan to run GEN-II. To solve this problem, we have developed a new technique in which convection, not diffusion, causes the mixing of the gas. This is the fifth advancement mentioned above. Finally, the fourth advancement (which chronologically came earlier), was the identification of a previously unrecognized relaxation rate. This discovery, made by Thad Walker’s group at the University of Wisconsin, has made it possible for us to understand the behavior of our targets at a level of detail that was not previously possible. For the first time, we are able to make measurements in our lab that allow us to predict with considerable accuracy the behavior that we see under full operating conditions.

In summary, the high-luminosity GEN-II target is based almost entirely on ideas that have either been demonstrated previously in Hall A, or ideas that have subsequently been tested in our lab. The “Transversity” experiment currently running in Hall A already has benefitted from polarizations as high as roughly 70%. With a few additional features, The GEN-II target will be able to run with 60% polarization even with a beam current of  $60\ \mu\text{A}$ , and an increased target length of 60 cm instead of 40 cm. The key new features that will make it possible to go to high currents include a cell that utilizes convection to enable rapid mixing, a metal target chamber, and a larger pumping chamber that will provide a bigger reservoir of polarized gas. The target will use ten spectrally-narrowed high-power diode-laser arrays. We note that some polarized  $^3\text{He}$  experiments at JLab have used as many as seven lasers in the past. In short, with the substantive advances that have occurred with polarized  $^3\text{He}$  targets in recent years, the GEN-II target is actually not a very ambitious jump at all. Rather, we are planning to take advantage of improvements that already exist.

#### 4.1 The principles behind the GEN-II target

The polarized  $^3\text{He}$  target is based on the technique of spin-exchange optical pumping which can be viewed as a two step process. In the first step, an alkali-metal vapor (in our case containing a mixture of potassium (K) and rubidium (Rb)) is polarized by optical pumping using radiation from a laser. In the second step, the polarized alkali-metal atoms collide with the  $^3\text{He}$  atoms, transferring their spin to the  $^3\text{He}$  nuclei through a hyperfine interaction. For the polarized  $^3\text{He}$  targets that have been used at JLab both the alkali vapor and the  $^3\text{He}$  are contained in sealed glass cells, an example of which is shown in Fig. 4.1.



Figure 4.1: Shown is one of the glass polarized  $^3\text{He}$  target cells used during GEN-I (E02-013).

If the diffusion time between the pumping chamber and the target chamber is fast enough that it can be neglected, the time dependence of the  $^3\text{He}$  polarization has a particularly simple form:

$$P_{\text{He}}(t) = P_{\text{Alk}} \frac{\gamma_{se}}{\gamma_{se}(1+X) + \Gamma} (1 - e^{-t(\gamma_{se} + \Gamma)}) \quad (4.1)$$

where  $P_{\text{He}}$  is the nuclear polarization of the  $^3\text{He}$ ,  $P_{\text{Alk}}$  is the polarization of the alkali-metal vapor,  $\gamma_{se}$  is the rate of spin-exchange rate between the  $^3\text{He}$  and the Rb, and  $\Gamma$  is the spin-relaxation rate of the  $^3\text{He}$  nuclei due to all other processes. The factor  $(1+X)$  accounts for what is now a well-established additional relaxation mechanism whose presence has been empirically established but whose origin is unknown[20]. The factor  $(1+X)$  has the form given because the additional relaxation mechanism has been seen to be roughly proportional to the alkali-metal number density. We note that the factor “ $X$ ” can be measured for any particular cell, and is one of the quantities that we have begun to measure for the various target cells that we produce.

The spin exchange rate can be written

$$\gamma_{se} = f_{pc}(k_{se}^{\text{K}}[\text{K}] + k_{se}^{\text{Rb}}[\text{Rb}]) \quad (4.2)$$

where  $f_{pc}$  is the fraction of  $^3\text{He}$  atoms that are located within the pumping chamber,  $k_{se}^{\text{K}}$  ( $k_{se}^{\text{Rb}}$ ) is the constant characterizing spin exchange between  $^3\text{He}$  and K(Rb), and  $[\text{K}]$  ( $[\text{Rb}]$ ) is the number density of K(Rb) atoms within the pumping chamber. It can be seen that in order to achieve high polarizations, we must have the relaxation rate  $\Gamma \ll \gamma_{se}$ . In principal, if the alkali-metal number density can be made arbitrarily high, the  $^3\text{He}$  polarization can approach the limiting value of  $P_{\text{Alk}}/(1+X)$ . In the past, the highest alkali-metal number density that could be maintained at something approaching 100% was strongly limited by the available laser power. By using alkali-hybrid mixtures and line-narrowed lasers, however, it is now possible to use very high alkali number densities.

The spin relaxation rate  $\Gamma$  contains several contributions and can be written

$$\Gamma = \Gamma_{wall} + \Gamma_{bulk} + \Gamma_{beam} \quad (4.3)$$

where  $\Gamma_{wall}$  is spin relaxation due to collisions between the  $^3\text{He}$  atoms and the container walls,  $\Gamma_{bulk}$  is spin relaxation due to  $^3\text{He}$ - $^3\text{He}$  collisions, and  $\Gamma_{beam}$  is spin relaxation due to the electron beam. For our target cells, the time constant associated with spin relaxation due to wall collisions and bulk effects,  $(\Gamma_{wall} + \Gamma_{bulk})^{-1}$ , is usually in the range of 20–40 hours. The beam depolarization rate has been studied both theoretically[21] and experimentally[22] and is given by

$$\Gamma_{beam} = (76,292 \text{ cm}^2/\text{g}) \rho_{\text{He}} L_{tc} J_{beam}/N_{\text{He}} \quad (4.4)$$

where  $\rho_{\text{He}}$  is the mass density of  $^3\text{He}$  in the target chamber,  $L_{tc}$  is the length of the target chamber,  $J_{beam}$  is the beam current in particles per unit time, and  $N_{\text{He}}$  is the total number of  $^3\text{He}$  atoms in the target. The time constant associated with with beam depolarization,  $(\Gamma_{beam})^{-1}$  was on the order of 100 hours during GEN-I. For GEN-II, for our proposed target configuration, it will be about 20 hours at  $60 \mu\text{A}$ . The GEN-II target incorporates two features that suppress depolarization due to the electron beam. First, convection-based mixing will be used to eliminate the polarization gradient between the pumping chamber and

the target chamber. Secondly, the pumping chamber will be substantially bigger, providing a large reservoir of polarized gas. The GEN-II target is based on a design in which 6.8 STP liters of gas are polarized. In contrast, the GEN-I target was based on a design in which 3 STP liters of gas were polarized.

## 4.2 The GEN-I polarized $^3\text{He}$ target and subsequent studies.

The figure of merit for the polarized  $^3\text{He}$  target during GEN-I was the highest that had ever been achieved by a polarized  $^3\text{He}$  target during an electron scattering experiment. The figure of merit for the current “Transversity” experiment is even higher still, but as only on-line data are available at this time (the experiment is still running at the time of this writing), we will restrict our comments on the Transversity targets to measurements made in our lab at UVa. The polarization achieved as a function of time for the GEN-I cell “Edna”, used for the majority of our data taking, is shown in Fig. 4.2. The polarization of the target was near or even above the 50% level for more than 50 days of running with beam currents that were typically about  $8\ \mu\text{A}$ . The polarization was well above the 40% level assumed in the original GEN-I proposal. Furthermore, while we ran at  $8\ \mu\text{A}$ , there is little question that the target would have performed well at  $12\ \mu\text{A}$ , the original design current. There were several factors that contributed to the high performance we observed, but central among them was the use of alkali-hybrid technology, the first time this approach was used in an electron scattering experiment.

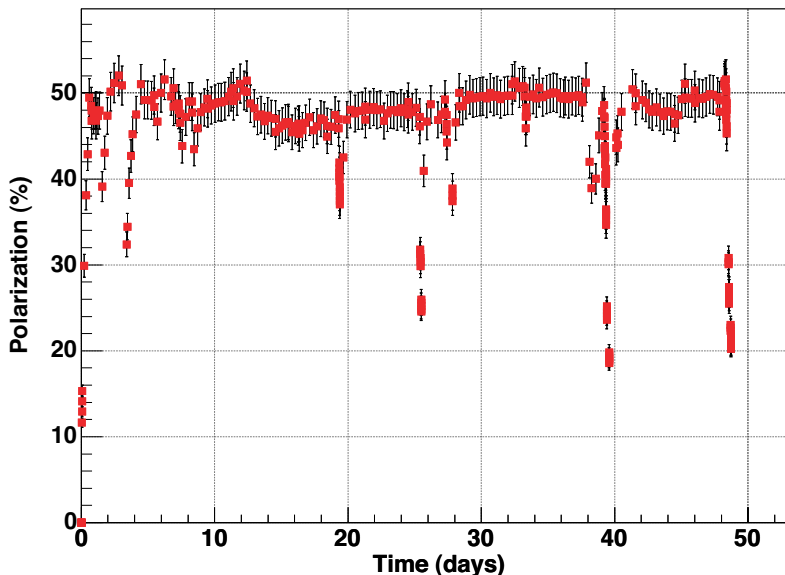


Figure 4.2: The polarization (in the target chamber) of Edna, the target cell with which the majority of the data were obtained during GEN-I (E02-013). The figure of merit of Edna is unprecedented in the history of the use of polarized  $^3\text{He}$  during an electron scattering experiment.

The physical configuration of the GEN-I target is illustrated in Fig. 4.3. The magnetic holding field for the polarized  $^3\text{He}$  was provided by a soft iron box that was magnetically excited using several sets of coils. This technique was economical in the use of space and was effective in reducing magnetic field gradients that were held below 10 mG/cm. The glass target cells were mounted on a movable target ladder (shown at right in the figure) that could be moved in and out of the beam as needed while continuously illuminating the target cell with laser light. The laser light was provided by several high-power diode-laser arrays that were outside of Hall A, and the light was transported to the target using optical fibers. While the exact geometry of the target for GEN-II has yet to be worked out in detail, the experience gained during GEN-I make it clear that we will have no difficulty operating in the high fringe fields of the Bigbite (electron arm) and Bigben (neutron arm sweeping magnet) magnets. This is particularly true because during GEN-II, as will be described more in the next section, we plan to relax the requirements for magnetic-field homogeneity for the target chamber. The GEN-II target will also use a fiber-optic-based optics system that builds on the system developed for GEN-I and currently in use for the Transversity experiment.

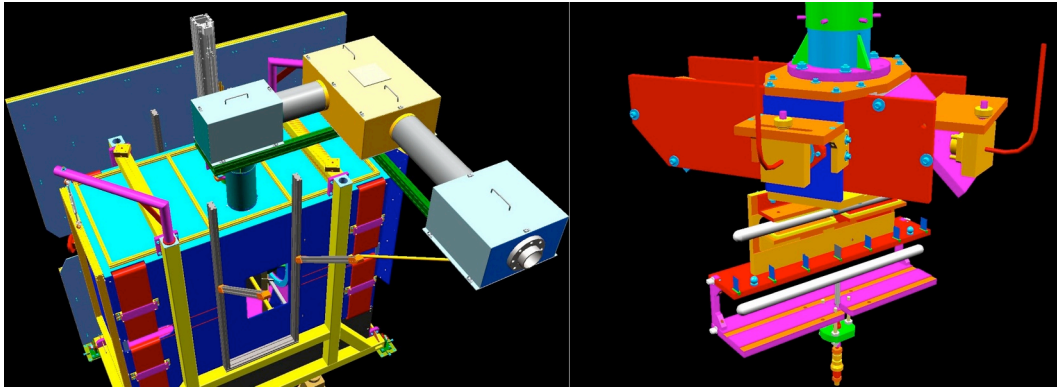


Figure 4.3: Shown are engineering renderings of the polarized  $^3\text{He}$  target used during GEN-I (E02-013). At left is an overview of the entire target, the largest feature being the soft iron box that, together with several coils used to magnetically energize the box, provided the magnetic holding field. Also visible on the left is the optics system (contained in three boxes mounted on top of the target) that provided circularly polarized laser light to the target. On the right is a close-up of the target ladder.

Despite the excellent performance achieved during GEN-I, there was an aspect of the GEN-I target-cell design that limited its performance. As discussed earlier, the pumping chamber, in which spin exchange takes place, and the target chamber, through which the electron beam travels, were connected by a single glass tube referred to as the “transfer tube”. Mixing between the two chambers occurs largely because of diffusion, and was characterized by a time constant of around 30–40 minutes. Historically the length of this time constant did not significantly limit the target’s performance, as the time constants characterizing polarization were much longer, around 20 hours. During GEN-I, however, because of the

very efficient use of laser light, it was possible to run the target in a mode in which the time constants characterizing the buildup of polarization were on the order of six hours. When the electron beam was incident on the target and thus causing depolarization, diffusion limited the rate at which the polarization in the target chamber could be replenished by the pumping chamber. This caused a significant polarization gradient between the pumping chamber and the target chamber. Fig. 4.2 shows the polarization as measured in the target chamber to be in the range of 47–52%. The polarization in the pumping chamber, however, was typically about 4.5% higher, or 51.5–56.5%.

The phenomenon of polarization gradients between the pumping chamber and the target chamber is something that we have now studied extensively at UVa. Even in the absence of the passage of an electron beam through the target chamber, the polarization gradient can be quite significant. An example of the effect is illustrated in Fig. 4.4, in which the polarization of both the pumping chamber (upper trace) and target chamber (lower trace) are shown as a function of time. In this particular test the cell was being run quite “hot”, that is, the time constant characterizing the spin-exchange time constant in the pumping chamber was around 4–5 hours. For this particular study, the gradient between the pumping chamber and the target chamber was around 7%. Polarization gradients have important implications if one is interested in running significantly higher beam currents. No matter how quickly gas can be polarized in the pumping chamber, the polarization in the target chamber will be limited if the gas does not move sufficiently quickly between the two chambers. We have solved this problem using a new approach based on convection that will be discussed more in the next section.

The study of polarization gradients illustrated in Fig. 4.4 is but one example of an extensive set of studies that have been performed at UVa in the time period following GEN-I and in preparation for the current set of polarized  $^3\text{He}$  experiments that are running in Hall A. Perhaps the most dramatic result of these studies was the establishment of polarizations that were consistently 70% or better. As mentioned earlier, there were two closely interacting factors that contributed to the big increase in target performance. One was the careful optimization of the hybrid technology using a new set of diagnostics that made it possible to measure not just the nuclear polarization of the  $^3\text{He}$ , but also the polarization and number densities of the Rb and K vapor. The other was the opportunity to use, for the first time, high-power diode-laser arrays with spectral widths of around 150 GHz, much narrower than than the roughly 1000 GHz spectral width of the lasers we had been using previously. With our optimized target cells, the new lasers, and our improved diagnostics guiding us, we saw huge improvement in target performance. Perhaps best of all, we have established the most detailed understanding of the physics occurring within our targets that we have ever had. This last point is critical, because it makes it straightforward to design an appropriate target for GEN-II.

### 4.3 The GEN-II High-Luminosity Target Cell

The high-luminosity GEN-II target cell represents a natural evolution of the GEN-I target cell, but incorporates two critical new features. First, instead of relying on diffusion to move

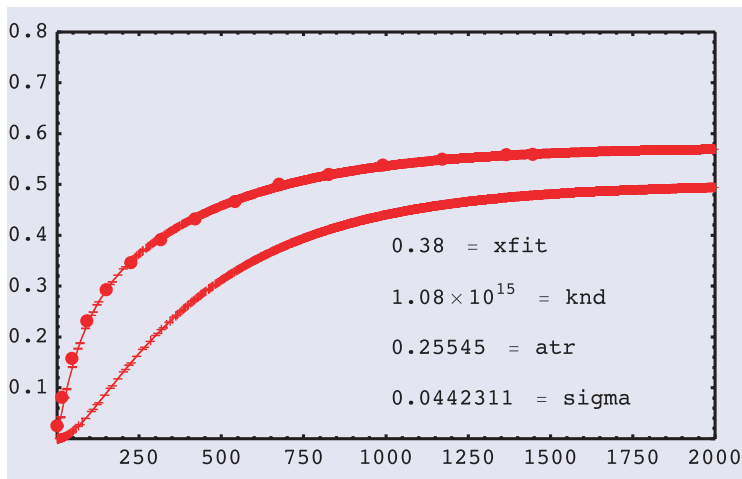


Figure 4.4: Data on the polarization of the target cell Simone as a function of time together with fits from a model that incorporates the effects of polarization gradients due to the limited rate of diffusion between the two chambers of the target cell. The upper trace shows the polarization in the pumping chamber and the lower trace shows the polarization in the target chamber. This figure illustrates the necessity of using convection instead of diffusion for targets that will be used in high-current electron beams.

gas between the pumping chamber and the target chamber, the new GEN-II cells will utilize convection. Second, the GEN-II target cells will be constructed out of both glass and metal. Specifically, the pumping chamber, in which the optical pumping and spin exchange take place, will be constructed out of glass, and the target chamber, through which the electron passes, will be constructed out of metal. Taken together, these two new features will make it possible to run the new target at very high currents. A rough conceptual design of the GEN-II target cell is shown in Fig. 4.5.

Ever since adopting alkali-hybrid technology, the rate at which  $^3\text{He}$  nuclei are being polarized in our targets is sufficient to compensate for a considerable amount of beam depolarization. As discussed in the last section, however, the rate at which polarized gas in the pumping chamber moves into the target chamber is limited by diffusion. Up to this point, all polarized  $^3\text{He}$  cells used at JLab have had a geometry similar to that of the cell depicted in Fig. 4.1 in which a single “transfer tube” connects the pumping chamber to the target chamber. In the GEN-II cell geometry, however, two transfer tubes are used. With this geometry, one of the transfer tubes can be heated in order to drive convection, and the gas in the two chambers can be mixed as quickly as is desired. In fact, once control is established over the mixing times, the pumping chamber and the target chamber can be physically separated by substantial distances, and even the magnetic fields of the two regions can be controlled independently.

The second feature that distinguishes the GEN-II cell from its predecessors is the use of a metallic target chamber. Our experience suggests that after something like 3–6 weeks of

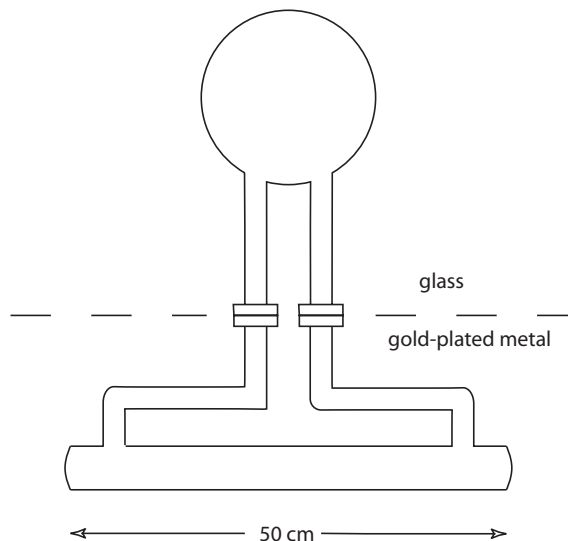


Figure 4.5: A conceptual design for the GEN-II target cell. Two transfers tubes connect the pumping chamber to the target chamber to make it possible to drive convection between the two cells. Also, the upper portion of the cell is made of glass, whereas the lower portion is made of metal, probably gold plated aluminum. The two sections are connected to one another using a flange system that captures a gasket made of either indium or gold.

beam in the range of  $5 - 8 \mu\text{A}$ , our all-glass target cells tend to explode. There is strong evidence that these catastrophic failures occur because of radiation damage, a problem that is certain to get much worse with substantially higher beam current. With a metal target chamber, however, the portion of the target that sees high radiation becomes quite robust. While we have not previously used metal in our  $^3\text{He}$  targets, it is important to point out that we have considerable experience using metal in the  $^3\text{He}$  polarizers that our group has constructed for medical imaging. In this work, we have found aluminum to be particularly benign from the perspective of spin relaxation. In our medical applications, however, the  $^3\text{He}$  nuclei spend less time in contact with metal than will be the case in the GEN-II target. We can glean some insight, however, from data taken by Ernst Otten's group at Mainz who measured a spin relaxation rate of  $1/6$  hours on aluminum, and  $1/20$  hours on gold[23]. Many of our target cells have intrinsic spin-relaxation times on the order of  $1/25$  hours, only marginally better than the wall relaxation induced by gold. Furthermore, in the GEN-II target, the  $^3\text{He}$  gas will be continually circulating because of the convection and will only reside in the metal target chamber something like 20% of the time. Our group has had quite favorable experience working with gold coating in optical pumping applications. Thus, based on both our own past experience as well as that of the group at Mainz, we are planning to use a gold-coated aluminum target chamber. For the glass-to-metal seal, we will employ a large glass flange coupled to a large metal flange that collectively will sandwich an o-ring. Our first choice would be an o-ring made of either gold or indium. We note, however, that the

cells we use for medical imaging all contain a polymer-based o-ring, and that is an acceptable solution. In summary, the challenges associated with the GEN-II target cell are not unlike the issues that we have already successfully faced in the context of medical imaging. Some development work will be required, but the important underlying materials issues, such as the spin-relaxation properties of the needed materials, have already been addressed.

#### 4.4 Convection Tests in a Prototype GEN-II Target Cell

As has already been emphasized, the success of the GEN-II target relies critically on our ability to circulate the polarized gas between the pumping chamber and the target chamber using convection. Indeed, this is the enabling technology for the GEN-II target, because it allows us to use a sealed cell with no moving parts. We thus felt that demonstrating our ability to drive convection would remove important uncertainties regarding the GEN-II target design. With this in mind, we constructed an all-glass sealed cell that approximates the basic geometry of the GEN-II target. The dimensions were chosen not to correspond to what we would ultimately like to build, but rather so that the test cell could be fabricated and tested using our existing apparatus. The resulting cell is shown in Fig. 4.6.

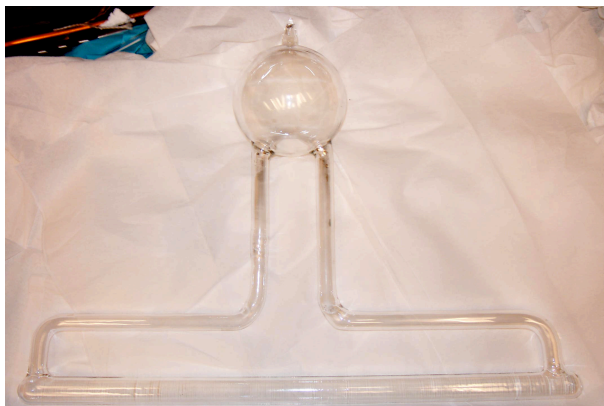


Figure 4.6: The first prototype “convection-driven target cell. Made entirely out of glass, this cell approximates the geometry of the proposed GEN-II target-cell geometry and is being used to prove the concept of mixing the gases of the pumping chamber and target chamber using convection.

To drive convection, a small hot-air driven heater was attached to the right-hand transfer tube leading out of the pumping chamber. To detect and characterize the convection, a small slug of gas was “tagged” by depolarizing it using a short pulse of resonant RF delivered by a small “zapper coil” that was wrapped around the left-hand transfer tube. The movement of the tagged slug of gas was tracked using a set of four “pick-up coils” that were spaced equally along the length of the target chamber. A photograph of the instrumented prototype cell is shown in Fig. 4.7.

Representative data from our tests are shown in Fig. 4.8. At  $t = 0$ , a pulse of RF was

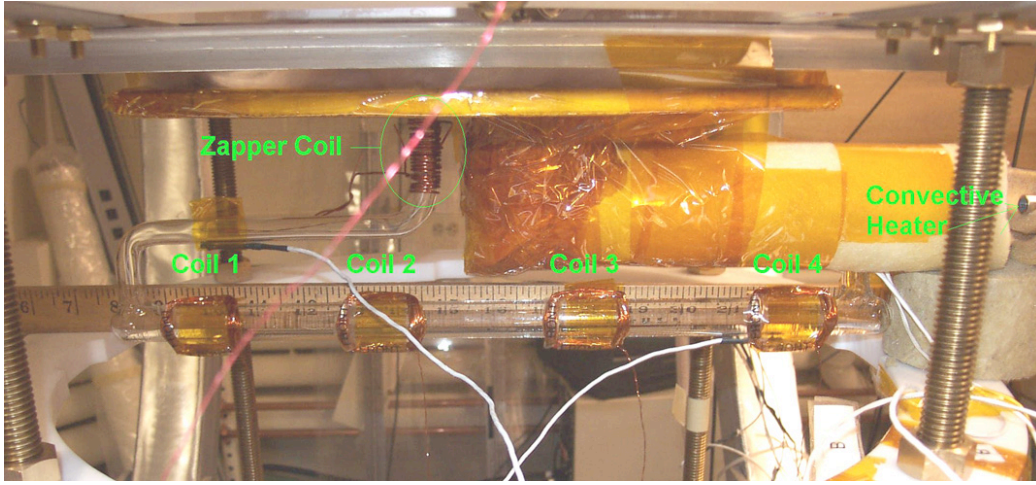


Figure 4.7: The prototype convection-driven target cell is shown instrumented for tests. As described in the text, a “zapper coil” is used to tag a slug of gas, and four pick-up coils monitor the movement of the tagged slug of gas through the target chamber. The speed of the convection is controlled using the “convection heater”.

delivered by the zapper coil, creating a depolarized slug of gas. The polarization of the gas passing through the four pick-up coils was monitored by making an NMR measurements every 5 seconds using the technique of adiabatic past passage. Each of the four coils clearly shows the passage of the depolarized gas as evidenced by the time dependence of the measured polarization. The first transient of reduced polarization appears in coil #1, the most upstream coil. Transients subsequently appear in each of coils #2–#4. It is interesting to note that the transient is relatively narrow as observed by coil #1, but broadens when observed by each successive coil. This is because diffusion is causing the slug of depolarization to spread out. Finally, we note that the data are of sufficient quality that we can compute the speed of the gas, which in this case, was around 20 cm/min.

We were able to control the speed with which the gas moved by adjusting the temperature of the heater attached to the left-hand transfer tube. The data shown in Fig. 4.8 were taken at 50°C. In Fig. 4.9, we show the results of measurements corresponding to setting our heater at temperatures between roughly 31°C and 67°C. Gas speeds in excess of 30 cm/min were observed. At such speeds, the gas in the target chamber will be replaced with new gas every two minutes, roughly 20 times faster than was the case during GEN-I. The implications of using convection-driven polarized  $^3\text{He}$  targets are quite profound. First, we are no longer limited in the speed with which we can replenish gas that has been depolarized by the electron beam. In addition, however, we are for the first time in a position to physically separate the region in which the  $^3\text{He}$  is polarized from the region in which the  $^3\text{He}$  serves as a target. Among other things, this provides considerable flexibility in the manner in which we generate magnetic holding fields, a matter that we will return to shortly.

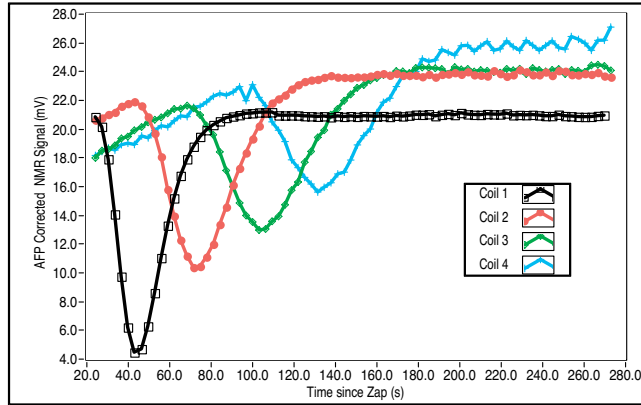


Figure 4.8: Shown are NMR signals from the four equally-spaced pick-up coils that were mounted on the target chamber as a function of time where  $t = 0$  corresponds to the creation of a depolarized slug of gas. Coil #1 was the most upstream coil, given the expected direction of flow. Transients corresponding to the passing of the depolarized gas are clearly visible (in the expected order) for each of the four coils.

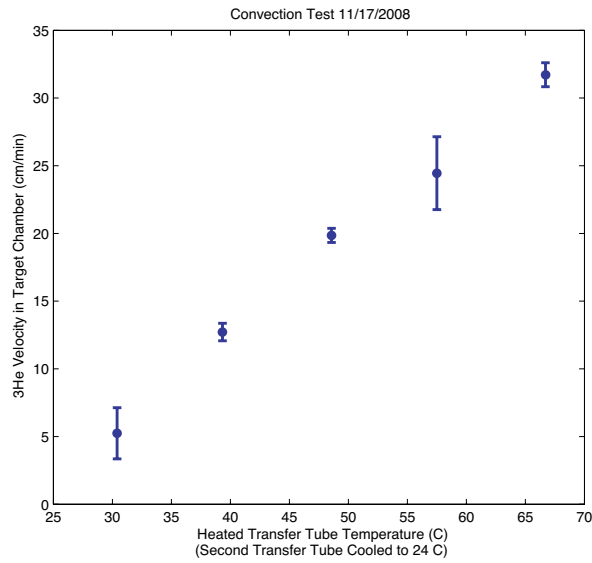


Figure 4.9: The measured speed of the gas moving through the target chamber is plotted as a function of the temperature of the “convection heater”. At 30 cm/s, the gas in the target chamber is replaced every 2 minutes, roughly 20 times faster than was the case during GEN-I.

## 4.5 Choosing Design Parameters for the GEN-II High-Luminosity Target

Using nothing more than the formalism presented earlier in the target section, it is straightforward to compute the expected performance for a given target design. Many of the inputs are quite unambiguous, such as target cell geometry,  $^3\text{He}$  density, and the expected depolarization due to interaction with the electron beam. Some of the inputs are specific to a given cell, such as the intrinsic spin-relaxation rate associated with a particular target cell, and the value of the so-called  $X$ -factor that characterizes the now well-established but poorly-understood relaxation mechanism that scales with alkali density. While these values are cell specific, we have measured them on a sufficient number of cells that we know with confidence what is achievable. Finally there is laser power, along with its implications for the maximum number density of alkali-metal atoms that can be maintained at very high polarization. In principle, the literature contains sufficient information to compute the required laser power for a particular set of operating conditions. We believe, however, that a more conservative approach is to formulate an estimate based on scaling.

We present in Fig. 4.10 (in the right-hand plot) the predicted performance for the GEN-II target. With a beam current of  $60\ \mu\text{A}$ , a target-chamber length of 60 cm, an intrinsic cell-specific spin-relaxation rate of  $1/25$  hrs, and an “ $X$ –” factor of 0.15, we predict a target polarization of 62%. For comparison, we have also calculated the expected polarization in a cell similar to what is currently being used in the “Transversity” experiment, but at  $60\ \mu\text{A}$ . Assuming diffusion to be infinitely fast, the expected polarization would be around 45%. The difference is that the GEN-II target incorporates a large reservoir of polarized gas in the pumping chamber, ensuring that the *fraction* of  $^3\text{He}$  nuclei being depolarized is smaller than would otherwise be the case. I note also that we have assumed in this comparison that the target chamber length of the Transversity-type cell was 60 cm (not the actual length of 40 cm) so that the absolute rate of beam depolarization would be the same for either target. Finally, when we calculate (not shown) the polarization that one would expect during the existing Transversity experiment, we get roughly 70%, just as observed, at least when the target polarization is not being rapidly flipped back and forth.

## 4.6 The Physical Configuration of the GEN-II Target

Having established the feasibility of running the GEN-II target at high luminosity, we include here a few comments on other aspects of the design.

First, the target chamber of the cell, that is, the metallic portion of the sealed polarized  $^3\text{He}$  target cell, will sit in a vacuum. While this has not been the practice at JLab, we note that the polarized  $^3\text{He}$  target cells used in both E-142 and E-154 (two experiments at SLAC that studied the spin structure of the neutron) sat in vacuum. At SLAC, however, this was quite challenging because it meant that even the oven that provides heat to the pumping chamber needed to sit in vacuum. The GEN-II target, however, will have a metal target chamber. It will thus be straightforward to have the target chamber sit in vacuum while the pumping chamber, along with optics, NMR components, etc., sit outside the vacuum.

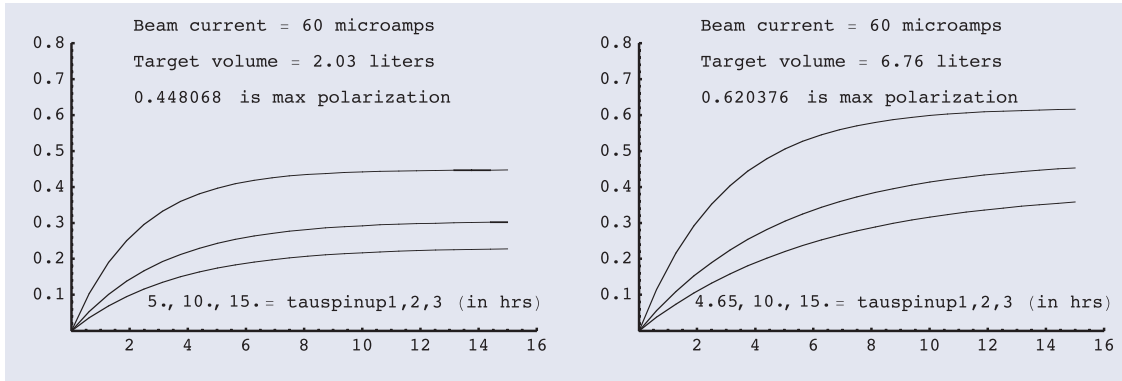


Figure 4.10: Shown are calculated “spin-up” curves for cells similar to those being used in the Transversity experiment (at left) and a cell with characteristics such as are planned for GEN-II (at right). For the GEN-II design, a polarization in excess of 60% is achieved at a beam current of  $60 \mu\text{A}$ .

Next, we comment on the magnetic holding fields. For GEN-II, we will only perform NMR measurements on the pumping chamber, not the target chamber. Historically, the magnetic field homogeneity requirements for the JLab polarized  $^3\text{He}$  targets have been driven by the need to minimize polarization losses during NMR measurements. This will still be true for the pumping chamber, but not for the target chamber. Assuming that we use a holding field of roughly 20 Gauss, the homogeneity requirement for the pumping chamber will be roughly 5–10 mG/cm. For the target chamber, however, the requirement will be roughly 200 mG/cm, a factor of 20–40 less demanding. Furthermore, we plan to control the magnetic field at the target chamber *independently* from the magnetic field in the pumping chamber. The two fields can even point in arbitrarily different directions. It will take roughly 2–3 minutes for gas to travel from the pumping chamber, down through the target chamber, and back into the pumping chamber. This is more than enough time for the spins to adiabatically follow the magnetic field through an arbitrary change in direction with negligible loss of polarization. One of us (Cates) used essentially this technique in an experiment at Los Alamos in which polarized muonic  $^3\text{He}$  was produced by stopping muons in polarized  $^3\text{He}$  gas[24]. The holding field for the  $^3\text{He}$  was adiabatically rotated once every two minutes by  $180^\circ$ , and no measurable loss of polarization was detected. Finally, since the magnetic field surrounding the target cell can point in an arbitrary direction, it can also be flipped at will. If done sufficiently smoothly, we believe it should be trivial to flip the magnetic field of the target chamber in ten seconds or less. For the SIDIS experiment, we plan to flip the target direction once every two minutes, losing less than 10% of the data-taking time in the process.

## Chapter 5

# Data Production and Analysis

The proposed experiment has basically 4 free parameters: the beam energy, the two spectrometer angles and the target polarization orientation. We intend to acquire data at 2 different beam energies, 8.8 and 11 GeV, in order to extract asymmetries at significantly different values of  $Q^2$  for the same point in  $x$  and  $z$ . The angles of the scattered electrons and hadrons are fixed at the most forward accessible values of  $30^\circ$  and  $14^\circ$  respectively. The target field magnet will be changed to get 4 target orientations perpendicular to the beam direction in order to cover the entire azimuthal phase space.

Asymmetries will be sampled in 2 dimensional space in the relevant variables  $(x, z)$ ,  $(x, P_\perp)$  and  $(z, P_\perp)$ . The quality of the data will assured by an experimental design that provides: good target performance, beam stability and luminosity, DAQ dead time below 20%, good tracking and excellent PID performance.

### 5.1 (SI)DIS Event Selection

For the analysis of the data and the selection of the SIDIS kinematic region, we intend to apply the kinematical cuts presented in Table 5.1. For comparison HERMES, and HallA 6 GeV SSA experiments nominal cuts are also presented together with the main motivations of their use.

### 5.2 Phase Space

Electrons are detected in the BB arm whose trigger will accept momenta from 1.2 GeV. Hadrons are detected by SBS, which includes the adapted HERMES RICH detector for hadron PID of  $\pi$  and  $K$ . For both beam energies, the BB spectrometer will be fixed at the central angle of 30 degree to match and to extend to high values (thanks to the high luminosity) the HERMES  $Q^2$  range. Correspondingly the SBS will be located at the central angle of 14 degree, the direction of the central photon momentum.

The angular and magnet field settings of the spectrometers are fixed (SBS magnet field will be reversed at least once for each setting to minimize systematics); 0.1 wide  $x$  bin have been considered. The central kinematics of the five  $x$  bins at 8.8 and 11 GeV beam energies

Table 5.1: DIS events selection, kinematical cuts and main motivation behind their use.

	Unit	Proposed Exp.	HERMES	Halla 6 GeV	Main reason
$Q^2$	GeV <sup>2</sup>	> 1	> 1	> 1.31	Larger than Nucleon Mass
$W$	GeV	2.3	> 3	> 2.33	Avoid resonance region
$W'$	GeV	> 1.5		> 1.5	Select fragmentation region
$y$		< 0.9	< 0.95		Avoid resonances
			$\geq 0.1$		Higher order QED suppressed
$z$		> 0.2	> 0.2		Acceptance effects
		< 0.7	< 0.7		Suppress target region
					Suppress exclusive production

Table 5.2: Kinematics at E=8.8 GeV for positive pions for different  $x$  bins. Reported are the central value and the approximate range.

$x$	$E'$ GeV	$P_\pi$ GeV	$W$ GeV	$Q^2$ GeV <sup>2</sup>	$z$	$P_\perp$ GeV
$0.20 \pm 0.05$	$1.25 \pm 0.16$	$3.40 \pm 1.09$	$3.48 \pm 0.08$	$2.93 \pm 0.34$	$0.45 \pm 0.25$	$0.61 \pm 0.24$
$0.30 \pm 0.05$	$1.65 \pm 0.21$	$3.19 \pm 1.02$	$3.21 \pm 0.09$	$4.01 \pm 0.33$	$0.45 \pm 0.25$	$0.49 \pm 0.21$
$0.40 \pm 0.05$	$2.07 \pm 0.23$	$3.02 \pm 0.97$	$2.91 \pm 0.09$	$5.03 \pm 0.32$	$0.45 \pm 0.25$	$0.37 \pm 0.18$
$0.50 \pm 0.05$	$2.44 \pm 0.26$	$2.77 \pm 0.88$	$2.62 \pm 0.10$	$5.95 \pm 0.33$	$0.44 \pm 0.24$	$0.28 \pm 0.14$
$0.60 \pm 0.05$	$2.65 \pm 0.22$	$2.53 \pm 0.79$	$2.40 \pm 0.06$	$6.70 \pm 0.33$	$0.41 \pm 0.24$	$0.23 \pm 0.13$

are presented in Table 5.2 and 5.3 respectively<sup>1</sup>. Pions and kaons of both charges will be acquired simultaneously.

The phase space distributions of the accepted particles has been determined using a Monte Carlo with realistic momentum and angular acceptance for BB and a box acceptance for SBS (angular acceptance is limited by the first tracker chamber). Figures 5.1, 5.2 and 5.3 show the phase space of the two detected particles momenta and angles and the relevant DIS variables range and correlations.

Finally, Fig. 5.4 shows the cumulated  $(Q^2, x)$  coverage of the two kinematics points at  $E = 11$  GeV and  $E = 8.8$  GeV.

In order to cover the full azimuthal range, the target will be operated at 4 spin orientations (swapping every  $\sim 10$  minutes, see section 3), perpendicular to the beam direction: left-right/horizontal and up-down/vertical.

The azimuthal phase spaces of  $\phi_s$  and  $\phi_\pi$  and their  $\pm$  linear combinations are shown in Figs. 5.5 5.6 for the up/vertical and up-down /vertical target configurations. Figures 5.7 and 5.8 show the cumulative phase spaces for all target configurations in polar and Cartesian views; the full angle coverage of  $\phi_s + \phi$  and  $\phi_s - \phi$  is clearly guaranteed, for different regions

<sup>1</sup>The last point at central  $x = 0.6$  and  $E = 8.8$  GeV will be probably dropped, being at the very edge of the acceptance

Table 5.3: Kinematics at E=11 GeV for positive pions for different  $x$  bins. Reported are the central value and the approximate range.

$x$	$E'$ GeV	$P_\pi$ GeV	$W$ GeV	$Q^2$ GeV <sup>2</sup>	$z$	$P_\perp$ GeV
$0.20 \pm 0.05$	$1.32 \pm 0.15$	$4.29 \pm 1.37$	$3.91 \pm 0.08$	$3.82 \pm 0.43$	$0.44 \pm 0.25$	$0.82 \pm 0.30$
$0.30 \pm 0.05$	$1.72 \pm 0.23$	$4.11 \pm 1.32$	$3.62 \pm 0.10$	$5.20 \pm 0.44$	$0.44 \pm 0.25$	$0.69 \pm 0.27$
$0.40 \pm 0.05$	$2.17 \pm 0.26$	$3.89 \pm 1.24$	$3.30 \pm 0.10$	$6.60 \pm 0.42$	$0.44 \pm 0.25$	$0.56 \pm 0.24$
$0.50 \pm 0.05$	$2.58 \pm 0.28$	$3.71 \pm 1.17$	$2.97 \pm 0.10$	$7.86 \pm 0.42$	$0.44 \pm 0.25$	$0.45 \pm 0.20$
$0.60 \pm 0.05$	$2.97 \pm 0.30$	$3.40 \pm 1.08$	$2.64 \pm 0.11$	$9.02 \pm 0.44$	$0.42 \pm 0.24$	$0.35 \pm 0.17$

of  $\phi_s$  and  $\phi$ .

### 5.3 Asymmetries

Assuming an unpolarized beam and a transversely polarized  ${}^3\text{He}$  target with polarization  $p_T$ , a neutron effective polarization  $p_n$  in  ${}^3\text{He}$ , and an unpolarized protons the SIDIS cross section can be written, according to eq. 1.1 as:

$$d\sigma(l_U + {}^3\text{He}^\uparrow \rightarrow l' + h + X) = d\sigma_{UU}^{2p} + d\sigma_{UU}^n + p_n p_T d\sigma_{UT}^n$$

where  $d\sigma_{UU}$  and  $d\sigma_{UT}$  have been defined in chapter 1.

The neutron Single Spin Asymmetry (UT) is defined by eq. 1.6 here represented:

$$A_{UT} = \frac{1}{|S_T|} \frac{d\sigma_{UT}}{d\sigma_{UU}}$$

which can be approximated, at leading twist 2, by the sum of three terms (eq. 1.7) modulated by different sin functions:

$$A_{UT} = A_{UT}^{\text{Collins}} \sin(\phi + \phi_S) + A_{UT}^{\text{Sivers}} \sin(\phi - \phi_S) + A_{UT}^{\text{Pretzelosity}} \sin(3\phi - \phi_S) \quad (5.1)$$

where the modulated terms are the Asymmetries or moments directly related to convolution of distribution and fragmentation functions as presented in chapter 1.

Experimentally, the number of events measured with a given polarization of the target ( $\phi_S$ ) is schematically given by:

$$N(\phi_S) = d\sigma(\phi_S) L(\phi_S)$$

where  $L(\phi_S)$  is the beam-target luminosity.

From the above, we have:

$$N^{3\text{He}}(\phi_S) = [d\sigma_{UU}^{2p} + d\sigma_{UU}^n + p_n p_T d\sigma_{UT}^n(\phi_S)] L(\phi_S)$$

and therefore, having two opposite target polarizations, we get in addition:

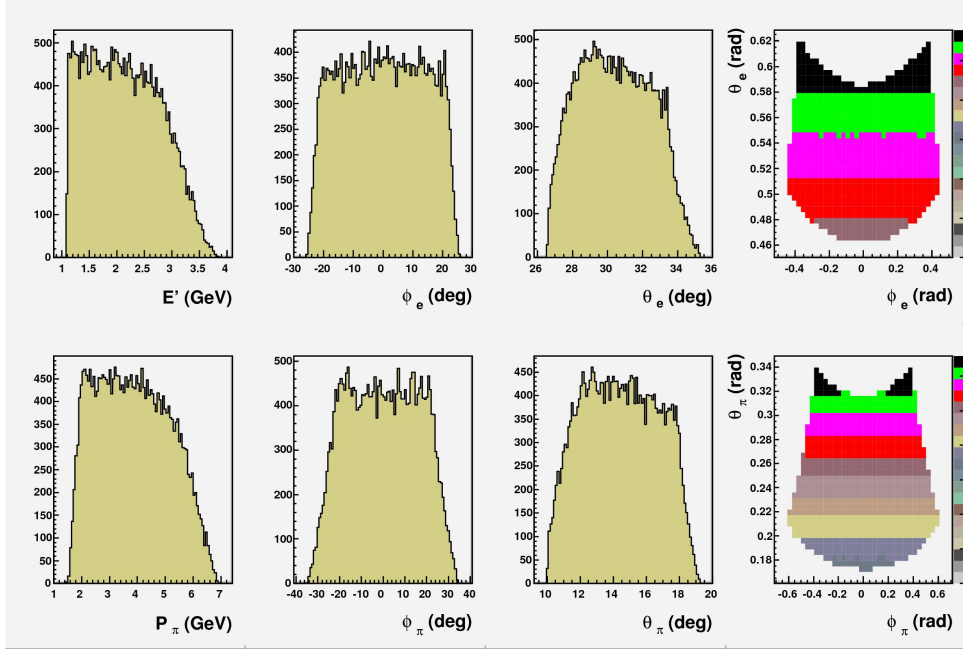


Figure 5.1: Phase space of the two detected particle momenta and angles, with the SIDIS cuts applied.

$$N^{3He}(\phi_S + \pi) = [d\sigma_{UU}^{2p} + d\sigma_{UU}^n - p_n p_T d\sigma_{UT}^n(\phi_S)] L(\phi_S + \pi)$$

The system of two equations can be solved:

$$A_{UT}^{exp} = \left( \frac{d\sigma_{UT}}{d\sigma_{UU}} \right)_{exp} = \frac{1}{f p_T p_n} \frac{N(\phi_S) L(\phi_S + \pi) - N(\phi_S + \pi) L(\phi_S)}{N(\phi_S) L(\phi_S + \pi) + N(\phi_S + \pi) L(\phi_S)}$$

where  $f = N_n / (N_n + N_{2p})$  ( $N = N_n + N_{2p}$ ) is the dilution factor (depends of phase space). The statistical error on the total asymmetry is therefore:

$$\sigma_A = \frac{1}{f p_T p_n \sqrt{N}} \quad (5.2)$$

with  $N \sim (N(\phi_S) + N(\phi_S + \pi))/2$

As a first approximation  $p_T$ ,  $p_n$ ,  $f$  do not depend on the direction of the target polarization.

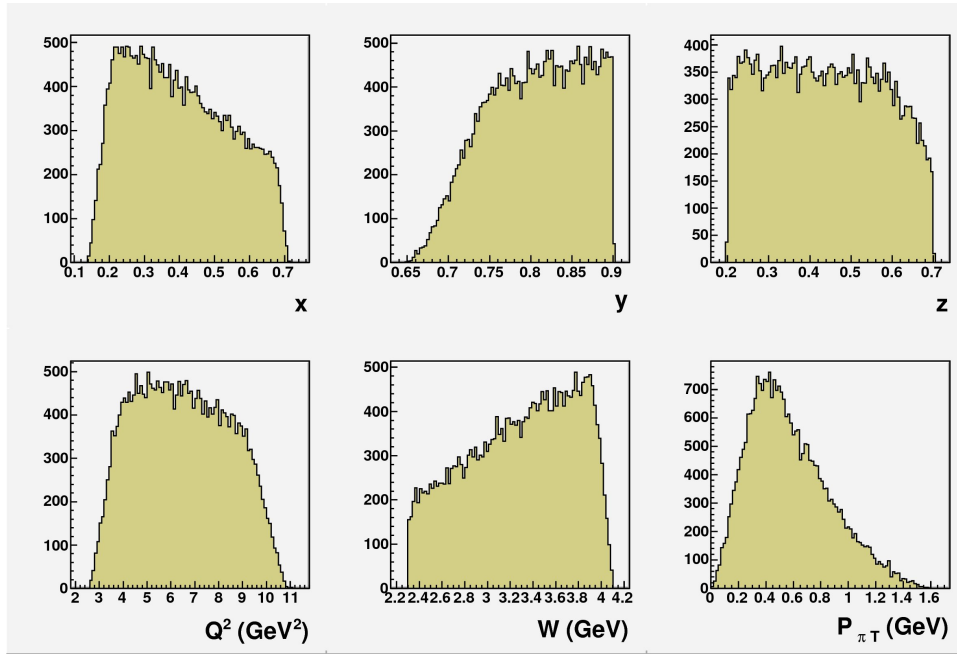


Figure 5.2: Phase space of the relevant variables, with the SIDIS cuts applied (for pions).

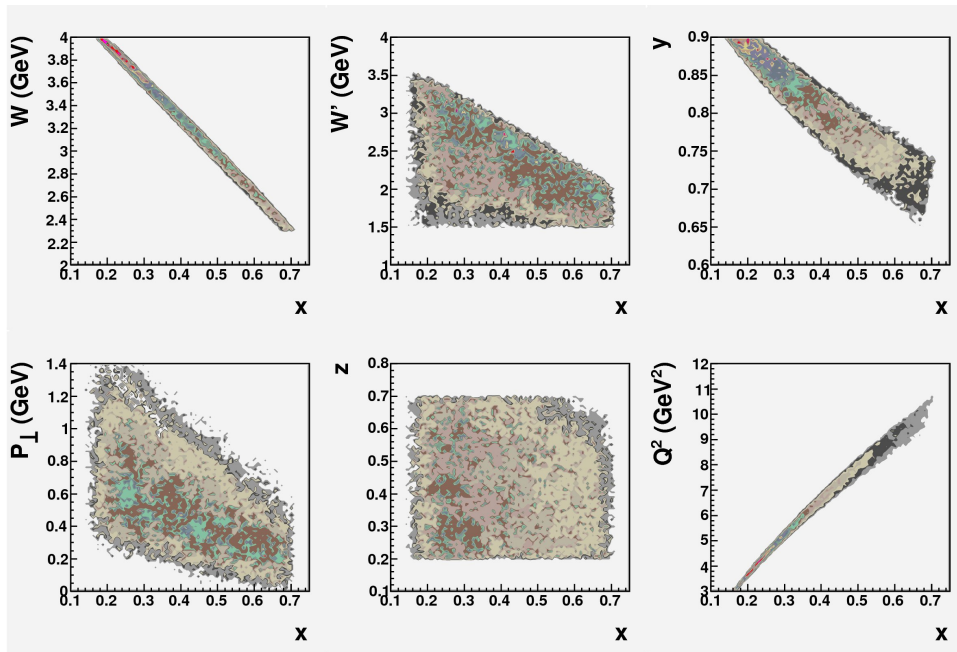


Figure 5.3: Correlated phase space of the relevant variables (for pions), with the SIDIS cuts applied.

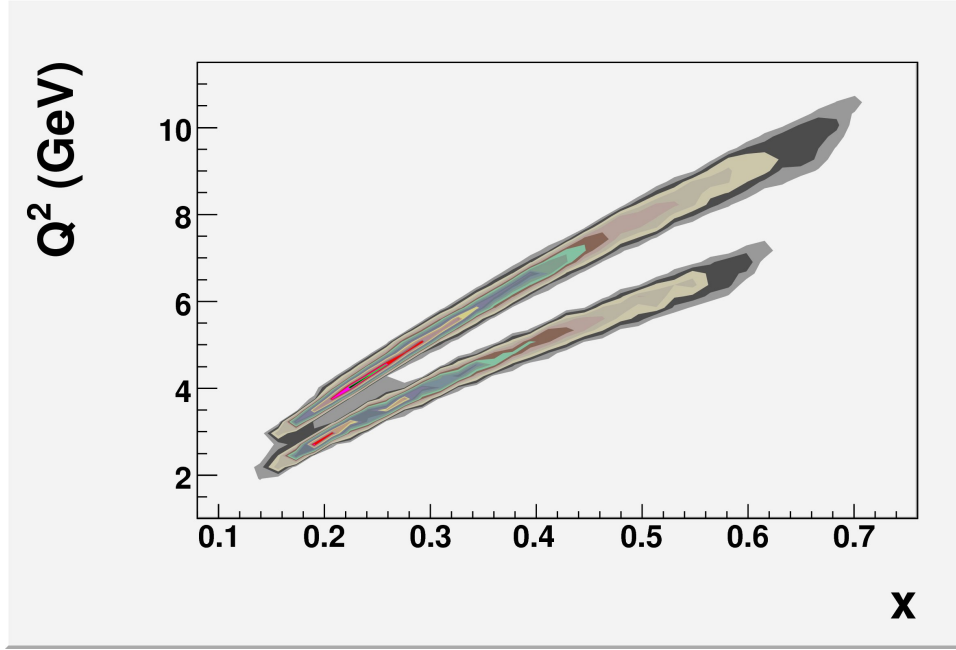


Figure 5.4: Cumulated  $E = 8.8$  and  $E = 11$  GeV  $Q^2$  vs  $x$  phase space (SIDIS cuts applied); upper band refer to  $E = 11$  GeV.

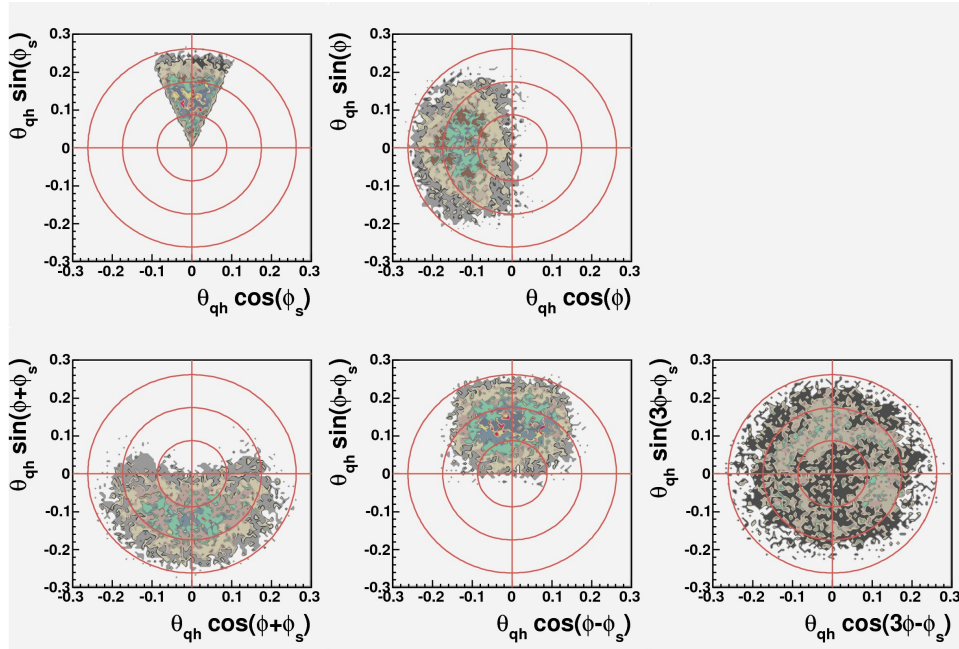


Figure 5.5: Azimuthal phase space for the vertical/up target settings, polar view ( $h = \pi$ )

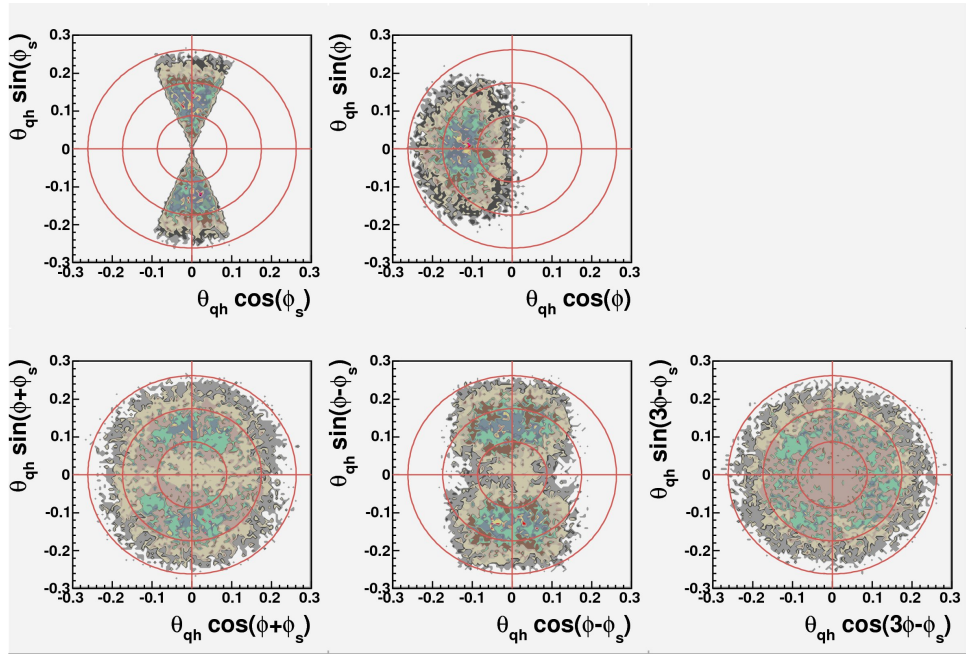


Figure 5.6: Azimuthal phase space for up/down vertical target settings, polar view ( $h = \pi$ )

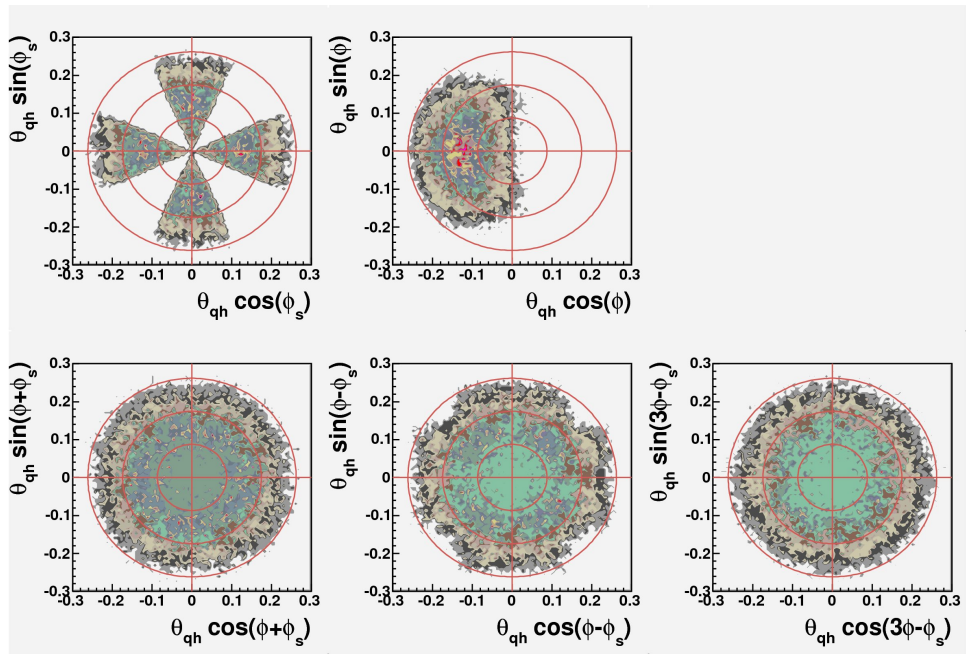


Figure 5.7: Azimuthal phase space for all target settings, polar view ( $h = \pi$ )

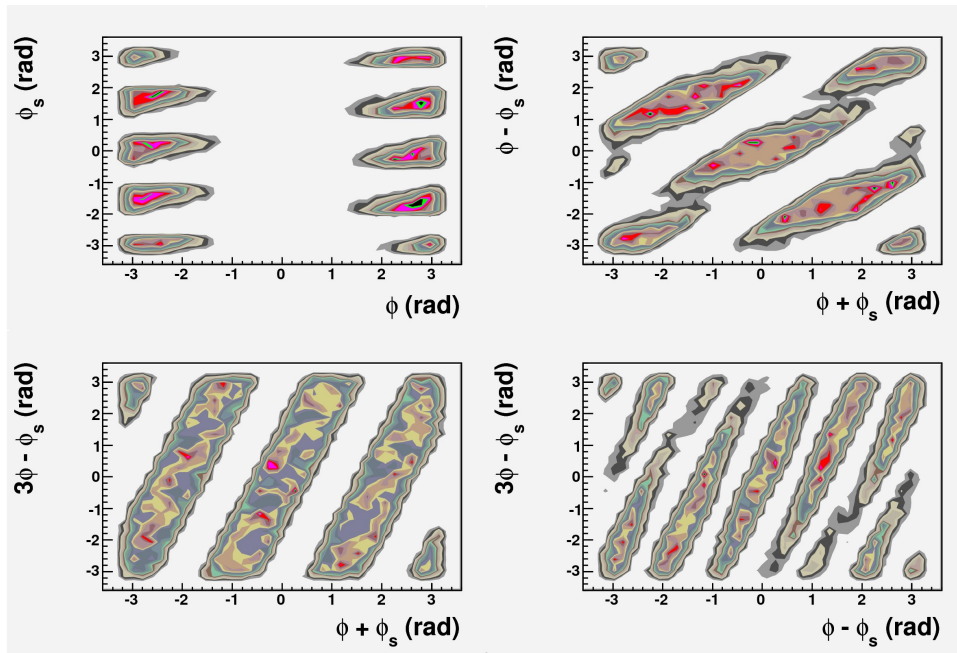


Figure 5.8: Azimuthal phase space for all target settings, Cartesian view ( $h = \pi$ ). Angle runs from  $-\pi$  to  $+\pi$ .

Table 5.4: Comparison of the relevant parameters affecting the statistical error of the physics asymmetry measurement, in HERMES and the proposed experiment ( $t$  is the time in sec)

Parameter	Symbol	Unit	HERMES (H)	Proposed Exp. (J)
dilution factor	$f$		1	0.20
Polarization	$p$	%	.8	.52
Cross Section $\sim s/Q^2$	$\sigma$	a.u.	4	1
Angular Acceptance	$\Delta\Omega$	mrs	$68 \times 68$	$50 \times 45$
Integrated Luminosity	$L \cdot t$	pb $^{-1}$	150.1	$3.9 \times t_J$

## 5.4 Rates

The expected statistical error on the physics asymmetry measurement (eq. 5.2) can be derived scaling from the “golden” standard of HERMES; in Table 5.4 we report the relevant parameters affecting the statistic errors.

Using Eq. 5.2, the time required to the proposed experiment to reach the statistical precision obtained by the HERMES experiment can be obtained using the relation

$$t_J = t_H \frac{L_H \Delta\Omega_H \sigma_H}{L_J \Delta\Omega_J \sigma_J} \left( \frac{f_H p_H}{f_J p_J} \right)^2$$

where  $H=$ HERMES,  $J=$ proposed experiment), and the symbol definitions (and values) are given in Table 5.4: this shows that we can match the HERMES precision in just  $t_J \sim 5$  hours. Therefore with 40 days of running at  $E = 11$  GeV we expect to get one order of magnitude better overall accuracy respect to HERMES.

The previous considerations have been confirmed by the following, more detailed, estimation which has been based on

- the CTEQ5M [26] parameterization of the unpolarized parton distribution functions (other recent parameterizations provide the same results within the accuracy),
- the DSS[27] parameterization of the unpolarized fragmentation functions,
- and recent analysis of Collins and Sivers FF as well as Transversity distribution of reference [43] and [42].

Moreover, the Kaon production has been normalized to the measured HERMES hadrons production[28] on  $H$  and  $D$  targets<sup>2</sup> which introduced the factors 1/4.1 and 1/6.7 in the  $K^+$  and  $K^-$  cross sections.

We adopted the conventional Gaussian factorization for the distribution and fragmentation functions:

$$f_q(x, Q^2, k_T) = f_q(x, Q^2) \frac{1}{\pi \langle k_T^2 \rangle} e^{-k_T^2 / \langle k_T^2 \rangle}$$

<sup>2</sup>The expected  $K/\pi$  rate is at the level of 20%.

Table 5.5: References to the tables in the current document that contain the estimation for the various processes, quantities and binning.

Table reference								
	8.8 GeV				11 GeV			
Cross Sections, Rates, Dilution	Inclusive							
	5.6				5.7			
Cross Sections, Rates, Dilution	Semi Inclusive 1D $x$ binning							
	$\pi^+$	$\pi^-$	$K^+$	$K^-$	$\pi^+$	$\pi^-$	$K^+$	$K^-$
					5.8	5.9	5.10	5.11
Events, Accuracy	Semi Inclusive 2D $(x, z)$ binning							
	5.12	5.14	5.16	5.18	5.13	5.15	5.17	5.19

and

$$D_q^h(z, Q^2, z^2 p_T^2) = D_q^h(z, Q^2) \frac{1}{\pi \langle p_T^2 \rangle} e^{-z^2 p_T^2 / \langle p_T^2 \rangle}$$

where  $k_T$  and  $z p_T$  are the initial and final quark transverse momentum, and  $\langle k_T^2 \rangle = 0.25$  (GeV/c)<sup>2</sup> and  $\langle p_T^2 \rangle = 0.20$  (GeV/c)<sup>2</sup> (from a fit of unpolarized data - Anselmino et al. Phys Rev D71 (2005) 074006)

The above approximation produces a  $P_\perp$  dependent weighting factor for the cross section:

$$\frac{1}{\pi (z^2 \langle p_T^2 \rangle + \langle k_T^2 \rangle)} e^{-\frac{|P_\perp|^2}{(z^2 \langle p_T^2 \rangle + \langle k_T^2 \rangle)}}$$

The presented rates and number of events are based on:

- Beam current of 40  $\mu$ A
- <sup>3</sup>He target 50 cm long with 11.5 atm pressure and 65% transverse polarization
- Neutron luminosity of 3.9 pb<sup>-1</sup>

Moreover, unstable particle decay is taken into account, assuming a target-SBS calorimeter distance of 6 m.

In the next tables, we move from inclusive to semi-inclusive calculations, and from 1-dimensional to 2-dimensional binning. For the sake of readability, we present a detailed estimation only for one kinematic point, while the statistics (number of events) and physics asymmetry accuracy are reported for all kinematics and particles in 2 dimensional binning  $(x, z)$ . The references to the tables is presented in Table 5.5.

We point out that the statistical accuracy in the physics  $\pi$  asymmetry is well below 1% for most of the  $(x, z)$  bins, for both beam energies, while it is at the level of 2-3 % for kaons.

Table 5.6:  $E = 8.8$  GeV: inclusive cross section and event rates on n and p, for  $3.9 \cdot 10^{36}$  neutron/cm<sup>2</sup>/s luminosity.

$E = 8.8$ GeV, Inclusive Cross Sections, Rates and Dilution						
$\langle x \rangle$	$d\sigma_I^n$ nb/sr/GeV	$N_{n(e,e')X}$ Hz	$d\sigma_I^p$ nb/sr/GeV	$N_{p(e,e')X}$ Hz	$N_{N(e,e')X}$ Hz	$f(n/{}^3He)$
0.20	2.24	209.31	3.02	282.02	773.35	0.27
0.30	1.19	116.10	1.88	182.93	481.96	0.24
0.40	0.62	49.55	1.12	89.07	227.68	0.22
0.50	0.31	19.57	0.61	39.35	98.27	0.20
0.60	0.15	4.36	0.32	9.59	23.54	0.19

Table 5.7:  $E = 11$  GeV: inclusive cross section and event rates on n and p, for  $3.9 \cdot 10^{36}$  neutron/cm<sup>2</sup>/s luminosity.

$E = 11$ GeV, Inclusive Cross Sections, Rates and Dilution						
$\langle x \rangle$	$d\sigma_I^n$ nb/sr/GeV	$R_{n(e,e')X}$ Hz	$d\sigma_I^p$ nb/sr/GeV	$R_{p(e,e')X}$ Hz	$R_{N(e,e')X}$ Hz	$f^{n/{}^3He}$
0.20	1.28	118.13	1.75	161.34	440.81	0.27
0.30	0.67	77.50	1.05	122.66	322.82	0.24
0.40	0.34	33.77	0.61	60.94	155.65	0.22
0.50	0.16	13.11	0.32	26.42	65.95	0.20
0.60	0.07	4.53	0.15	10.17	24.86	0.18

Table 5.8:  $E = 11$  GeV,  $\pi^+$  seminclusive cross section and event rates on n and p, for  $3.9 \cdot 10^{36}$  neutron/cm<sup>2</sup>/s luminosity.

$E = 11$ GeV, $\pi^+$ Semi-Inclusive Cross Sections, Rates and Dilution						
$\langle x \rangle$	$d\sigma_{\pi^+}^n$ nb/sr <sup>2</sup> /GeV <sup>2</sup>	$R_{n(e,e'\pi^+)X}$ Hz	$d\sigma_{\pi^+}^p$ nb/sr <sup>2</sup> /GeV <sup>2</sup>	$R_{p(e,e'\pi^+)X}$ Hz	$R_{{}^3He(e,e'\pi^+)X}$ Hz	$f_{\pi^+}(n/{}^3He)$
0.20	0.77	3.54	1.24	5.69	14.93	0.24
0.30	0.40	2.25	0.76	4.30	10.85	0.21
0.40	0.21	1.01	0.46	2.29	5.58	0.18
0.50	0.09	0.41	0.25	1.09	2.59	0.16
0.60	0.04	0.13	0.12	0.40	0.94	0.14

Table 5.9:  $E = 11$  GeV,  $\pi^-$  semiinclusive cross section and event rates on n and p, for  $3.9 \cdot 10^{36}$  neutron/cm<sup>2</sup>/s luminosity.

$E = 11$ GeV, $\pi^-$ Semi-Inclusive Cross Sections, Rates and Dilution						
$\langle x \rangle$	$d\sigma_{\pi^-}^n$ nb/sr <sup>2</sup> /GeV <sup>2</sup>	$R_{n(e,e'\pi^-)X}$ Hz	$d\sigma_{\pi^-}^p$ nb/sr <sup>2</sup> /GeV <sup>2</sup>	$R_{p(e,e'\pi^-)X}$ Hz	$R_{^3He(e,e'\pi^-)X}$ Hz	$f_{\pi^-}(n/{}^3He)$
0.20	0.70	3.10	0.74	3.27	9.64	0.32
0.30	0.38	2.21	0.44	2.56	7.32	0.30
0.40	0.19	0.98	0.24	1.19	3.36	0.29
0.50	0.10	0.41	0.13	0.53	1.47	0.28
0.60	0.05	0.15	0.06	0.20	0.56	0.27

Table 5.10:  $E = 11$  GeV,  $K^+$  semiinclusive cross section and event rates on n and p, for  $3.9 \cdot 10^{36}$  neutron/cm<sup>2</sup>/s luminosity.

$E = 11$ GeV, $K^+$ Semi-Inclusive Cross Sections, Rates and Dilution						
$\langle x \rangle$	$d\sigma_{K^+}^n$ nb/sr <sup>2</sup> /GeV <sup>2</sup>	$R_{n(e,e'K^+)X}$ Hz	$d\sigma_{K^+}^p$ nb/sr <sup>2</sup> /GeV <sup>2</sup>	$R_{p(e,e'K^+)X}$ Hz	$R_{^3He(e,e'K^+)X}$ Hz	$f_{K^+}(n/{}^3He)$
0.20	0.19	0.72	0.31	1.16	3.04	0.24
0.30	0.10	0.47	0.19	0.89	2.26	0.21
0.40	0.05	0.20	0.11	0.45	1.10	0.18
0.50	0.02	0.08	0.06	0.21	0.50	0.16
0.60	0.01	0.03	0.03	0.08	0.19	0.14

Table 5.11:  $E = 11$  GeV,  $K^-$  semiinclusive cross section and event rates on n and p, for  $3.9 \cdot 10^{36}$  neutron/cm<sup>2</sup>/s luminosity.

$E = 11$ GeV, $K^-$ Semi-Inclusive Cross Sections, Rates and Dilution						
$\langle x \rangle$	$d\sigma_{K^-}^n$ nb/sr <sup>2</sup> /GeV <sup>2</sup>	$R_{n(e,e'K^-)X}$ Hz	$d\sigma_{K^-}^p$ nb/sr <sup>2</sup> /GeV <sup>2</sup>	$R_{p(e,e'K^-)X}$ Hz	$R_{^3He(e,e'K^-)X}$ Hz	$f_{K^-}(n/{}^3He)$
0.20	0.10	0.39	0.11	0.42	1.23	0.32
0.30	0.06	0.26	0.06	0.30	0.85	0.30
0.40	0.03	0.12	0.04	0.15	0.42	0.29
0.50	0.02	0.05	0.02	0.07	0.19	0.28
0.60	0.01	0.02	0.01	0.02	0.07	0.27

Table 5.12:  $E = 8.8$  GeV,  $\pi^+$  total events and corresponding asymmetry accuracy for  $3.9 \cdot 10^{36}$  neutron/cm<sup>2</sup>/s luminosity, single target setting, 20 days of running, both  $x$  and  $z$  binning (bin width  $0.1 \times 0.1$ ).

$E = 8.8$ GeV, $\pi^+$ Semi-Inclusive Event Statistics and Asymmetry Accuracy												
$\langle x \rangle$	$\langle z \rangle = 0.25$		$\langle z \rangle = 0.35$		$\langle z \rangle = 0.45$		$\langle z \rangle = 0.55$		$\langle z \rangle = 0.65$		full $z$ range	
	$N_{\pi^+}$ kEvts	$\sigma_A$ %	$N_{\pi^+}$ kEvts	$\sigma_A$ %								
0.20	14538	0.19	8636	0.26	4865	0.35	2699	0.47	1576	0.63	32313	0.13
0.30	9160	0.28	5509	0.37	3150	0.50	1968	0.64	1124	0.87	20910	0.19
0.40	4130	0.46	2548	0.63	1482	0.84	886	1.10	525	1.48	9571	0.32
0.50	2026	0.75	1252	1.03	621	1.50	429	1.83	211	2.70	4540	0.53
0.60	575	1.57	308	2.33	162	3.31	104	4.22	25	8.96	1175	1.16

Table 5.13:  $E = 11$  GeV,  $\pi^+$  total events and corresponding asymmetry accuracy for  $3.9 \cdot 10^{36}$  neutron/cm<sup>2</sup>/s luminosity, single target setting, 40 days of running, both  $x$  and  $z$  binning (bin width  $0.1 \times 0.1$ ).

$E = 11$ GeV, $\pi^+$ Semi-Inclusive Event Statistics and Asymmetry Accuracy												
$\langle x \rangle$	$\langle z \rangle = 0.25$		$\langle z \rangle = 0.35$		$\langle z \rangle = 0.45$		$\langle z \rangle = 0.55$		$\langle z \rangle = 0.65$		full $z$ range	
	$N_{\pi^+}$ kEvts	$\sigma_A$ %	$N_{\pi^+}$ kEvts	$\sigma_A$ %								
0.20	29766	0.13	17045	0.18	10030	0.24	5405	0.33	3264	0.44	65510	0.09
0.30	18960	0.19	11207	0.26	6353	0.35	3801	0.46	2320	0.60	42640	0.13
0.40	8832	0.32	5215	0.44	3156	0.58	1730	0.79	1084	1.03	20017	0.22
0.50	4126	0.53	2535	0.72	1358	1.01	848	1.30	437	1.88	9306	0.37
0.60	1099	1.13	592	1.68	361	2.22	206	3.00	51	6.25	2310	0.83

Table 5.14:  $E = 8.8$  GeV,  $\pi^-$  total events and corresponding asymmetry accuracy for  $3.9 \cdot 10^{36}$  neutron/cm<sup>2</sup>/s luminosity, single target setting, 20 days of running, both  $x$  and  $z$  binning (bin width  $0.1 \times 0.1$ ).

$E = 8.8$ GeV, $\pi^-$ Semi-Inclusive Event Statistics and Asymmetry Accuracy												
$\langle x \rangle$	$\langle z \rangle = 0.25$		$\langle z \rangle = 0.35$		$\langle z \rangle = 0.45$		$\langle z \rangle = 0.55$		$\langle z \rangle = 0.65$		full $z$ range	
	$N_{\pi^-}$ kEvts	$\sigma_A$ %	$N_{\pi^-}$ kEvts	$\sigma_A$ %								
0.20	10863	0.18	5423	0.23	2993	0.31	1532	0.42	869	0.53	21681	0.12
0.30	6520	0.24	2988	0.33	1770	0.42	924	0.56	504	0.71	12705	0.17
0.40	3290	0.36	1486	0.49	794	0.64	462	0.82	246	1.02	6279	0.25
0.50	1489	0.56	651	0.75	378	0.94	199	1.25	81	1.77	2797	0.38
0.60	374	1.15	155	1.56	94	1.91	50	2.52	10	5.11	683	0.79

Table 5.15:  $E = 11$  GeV,  $\pi^-$  total events and corresponding asymmetry accuracy for  $3.9 \cdot 10^{36}$  neutron/cm<sup>2</sup>/s luminosity, single target setting, 40 days of running, both  $x$  and  $z$  binning (bin width  $0.1 \times 0.1$ ).

$E = 11$ GeV, $\pi^-$ Semi-Inclusive Event Statistics and Asymmetry Accuracy												
$\langle x \rangle$	$\langle z \rangle = 0.25$		$\langle z \rangle = 0.35$		$\langle z \rangle = 0.45$		$\langle z \rangle = 0.55$		$\langle z \rangle = 0.65$		full $z$ range	
	$N_{\pi^-}$	$\sigma_A$	$N_{\pi^-}$	$\sigma_A$								
	kEvts	%	kEvts	%								
0.20	17460	0.14	9315	0.18	4390	0.25	2537	0.33	1044	0.48	34746	0.09
0.30	13025	0.17	6413	0.23	3165	0.31	1864	0.40	843	0.55	25310	0.12
0.40	5772	0.27	2907	0.35	1507	0.47	882	0.59	395	0.81	11463	0.18
0.50	2494	0.43	1271	0.54	676	0.71	350	0.94	164	1.25	4956	0.28
0.60	1073	0.69	516	0.86	262	1.15	124	1.60	45	2.39	2021	0.46

Table 5.16:  $E = 8.8$  GeV,  $K^+$  total events and corresponding asymmetry accuracy for  $3.9 \cdot 10^{36}$  neutron/cm<sup>2</sup>/s luminosity, single target setting, 20 days of running, both  $x$  and  $z$  binning (bin width  $0.1 \times 0.1$ ).

$E = 8.8$ GeV, $K^+$ Semi-Inclusive Event Statistics and Asymmetry Accuracy												
$\langle x \rangle$	$\langle z \rangle = 0.25$		$\langle z \rangle = 0.35$		$\langle z \rangle = 0.45$		$\langle z \rangle = 0.55$		$\langle z \rangle = 0.65$		full $z$ range	
	$N_{K^+}$	$\sigma_A$	$N_{K^+}$	$\sigma_A$								
	kEvts	%	kEvts	%								
0.20	2783	0.43	1633	0.59	902	0.80	498	1.09	302	1.43	6119	0.30
0.30	1785	0.62	988	0.88	587	1.16	370	1.47	195	2.09	3925	0.43
0.40	901	1.00	475	1.46	283	1.92	183	2.42	94	3.51	1935	0.71
0.50	367	1.77	212	2.50	131	3.25	78	4.28	30	7.09	818	1.24
0.60	121	3.40	62	5.20	30	7.72	14	11.64	3	27.07	229	2.60

Table 5.17:  $E = 11$  GeV,  $K^+$  total events and corresponding asymmetry accuracy for  $3.9 \cdot 10^{36}$  neutron/cm<sup>2</sup>/s luminosity, single target setting, 40 days of running, both  $x$  and  $z$  binning (bin width  $0.1 \times 0.1$ ).

$E = 11$ GeV, $K^+$ Semi-Inclusive Event Statistics and Asymmetry Accuracy												
$\langle x \rangle$	$\langle z \rangle = 0.25$		$\langle z \rangle = 0.35$		$\langle z \rangle = 0.45$		$\langle z \rangle = 0.55$		$\langle z \rangle = 0.65$		full $z$ range	
	$N_{K^+}$ kEvts	$\sigma_A$ %	$N_{K^+}$ kEvts	$\sigma_A$ %								
0.20	4917	0.33	3017	0.44	1541	0.62	907	0.82	495	1.13	10878	0.23
0.30	3289	0.46	2070	0.61	1207	0.81	680	1.09	367	1.53	7612	0.31
0.40	1731	0.72	976	1.02	579	1.35	328	1.82	182	2.52	3796	0.51
0.50	757	1.23	450	1.72	255	2.34	151	3.09	71	4.69	1684	0.87
0.60	330	2.12	197	3.01	111	4.09	56	5.91	18	10.96	712	1.53

Table 5.18:  $E = 8.8$  GeV,  $K^-$  total events and corresponding asymmetry accuracy for  $3.9 \cdot 10^{36}$  neutron/cm<sup>2</sup>/s luminosity, single target setting, 7 days of running, both  $x$  and  $z$  binning (bin width  $0.1 \times 0.1$ ).

$E = 8.8$ GeV, $K^-$ Semi-Inclusive Event Statistics and Asymmetry Accuracy												
$\langle x \rangle$	$\langle z \rangle = 0.25$		$\langle z \rangle = 0.35$		$\langle z \rangle = 0.45$		$\langle z \rangle = 0.55$		$\langle z \rangle = 0.65$		full $z$ range	
	$N_{K^-}$ kEvts	$\sigma_A$ %	$N_{K^-}$ kEvts	$\sigma_A$ %								
0.20	1287	0.51	625	0.69	333	0.92	188	1.20	100	1.56	2533	0.35
0.30	751	0.72	375	0.94	193	1.27	117	1.59	56	2.13	1492	0.48
0.40	406	1.04	183	1.39	94	1.87	50	2.49	26	3.17	759	0.71
0.50	150	1.77	80	2.14	41	2.87	22	3.77	8	5.59	301	1.15
0.60	45	3.34	23	4.09	11	5.68	5	8.26	0	24.98	84	2.27

Table 5.19:  $E = 11$  GeV,  $K^-$  total events and corresponding asymmetry accuracy for  $3.9 \cdot 10^{36}$  neutron/cm<sup>2</sup>/s luminosity, single target setting, 40 days of running, both  $x$  and  $z$  binning (bin width  $0.1 \times 0.1$ ).

$E = 11$ GeV, $K^-$ Semi-Inclusive Event Statistics and Asymmetry Accuracy												
$\langle x \rangle$	$\langle z \rangle = 0.25$		$\langle z \rangle = 0.35$		$\langle z \rangle = 0.45$		$\langle z \rangle = 0.55$		$\langle z \rangle = 0.65$		full $z$ range	
	$N_{K^-}$ kEvts	$\sigma_A$ %	$N_{K^-}$ kEvts	$\sigma_A$ %								
0.20	2234	0.39	1039	0.54	563	0.71	318	0.93	151	1.27	4305	0.27
0.30	1573	0.50	786	0.65	377	0.91	230	1.13	107	1.55	3074	0.34
0.40	665	0.81	361	0.99	194	1.30	101	1.75	45	2.40	1366	0.52
0.50	322	1.21	161	1.51	79	2.07	39	2.82	18	3.80	619	0.81
0.60	135	1.94	62	2.47	30	3.41	14	4.70	4	8.46	245	1.32

## 5.5 Extraction of the Sivers and Collins Asymmetries

The Collins and Sivers asymmetries are extracted from the measured total asymmetry by a proper fit in the azimuthal sinusoidal modulations (see eq. 5.1).

For each kinematic bin, the total measured asymmetry is sampled at various  $\phi^i$  and  $\phi_S^j$  bins, obtaining the following relations:

$$A_{UT}^{exp}(\phi^i, \phi_S^j) = A_{UT}^{Collins,exp} \sin(\phi^i + \phi_S^j) + A_{UT}^{Sivers,exp} \sin(\phi^i - \phi_S^j) + C$$

where the Collins and Sivers amplitudes (and  $C$ , which should vanish) represent the unknown parameters to be estimated by a linear fit<sup>3</sup>. In this respect the full coverage of the Sivers ( $\phi - \phi_S$ ) and Collins ( $\phi + \phi_S$ ) angles (achieved by the proposed experiment, as shown in section 5.2) is rather important. Different approaches have been developed for the asymmetries extraction ([29]), that can be applied to the present experiment data.

Independently from the chosen technique, the errors on both asymmetries ( $\sigma_{A^\pm}$  for short) can be estimated as variance of the parameters in the standard linear least square method:

$$\sigma_{A^\pm} = \frac{1}{\Delta} \cdot \sum_{i,j} \frac{\sin^2(\phi^i \pm \phi_S^j)}{\sigma_{A(i,j)}^2}$$

with

$$\Delta = \left| \sum_{i,j} \frac{\sin^2(\phi^i + \phi_S^j)}{\sigma_{A(i,j)}^2} \sum_{i,j} \frac{\sin^2(\phi^i - \phi_S^j)}{\sigma_{A(i,j)}^2} - \left( \sum_{i,j} \frac{\sin(\phi^i + \phi_S^j) \sin(\phi^i - \phi_S^j)}{\sigma_{A(i,j)}^2} \right)^2 \right|$$

where  $A(i, j) = A_{UT}^{exp}(\phi^i, \phi_S^j)$ .

Replacing the sum on the modulation sin's by the integral in  $2\pi$  and assuming a constant error  $\sigma_A^{bin} \sim \sigma_A \sqrt{N} / \sqrt{N/n_b} = \sigma_A \sqrt{n_b}$  on the binned  $A(i, j)$  (scaled by the number of bins  $n_b$ ), where  $\sigma_A$  is quoted in the tables of section 5.4. Under these assumptions, uncertainties on both asymmetries are equal to  $\sigma_{A^{C/S}} \sim \sigma_A \sqrt{n_b} / (\pi\sqrt{2}) \sim 2\sigma_A$ , for a reasonable number of bins  $n_b \sim 64 \div 100$ .

## 5.6 Systematics Errors Analysis

Several possible sources of systematic errors may contribute to the measured asymmetries. The analysis of the proposed experiment will benefit of the experience gained in HERMES and in the E06-010 6 GeV Hall A Transversity ([35]) experiments.

In fact, the proposed experiment intends to use an apparatus that can be considered a mixture of HERMES and E06-010:

- double open spectrometer similar to HERMES,

---

<sup>3</sup>Suppressed asymmetries modulated by the corresponding sin or cos functions can be included in the expression and considered as additional parameters of the fit.

- one of the spectrometer already used in the 6 GeV experiment ad JLab (with reconfigured tracking and trigger),
- almost identical hadron identification of HERMES.
- similar or better momentum and angular resolution
- similar spin flip frequency of HERMES (100 s or so), which suppress systematics

On one side large part of the analysis that will be carried on for the 6 GeV experiment can be applied to the current experiment and on the other side some of the HERMES achievements in extracting the asymmetries can be easily adapted.

In general, the physics asymmetry (eq. 5.3) is affected by systematics that come from:

1. the accuracy on the knowledge of luminosity, target polarization, kinematic variables and particle identification
2. the fluctuations and drift of the experimental conditions (e.g. detector efficiency)
3. the random background events entering the coincidence.
4. the approximations behind the (eq. 5.3), that is:
  - Nuclear effects (the neutron is not free) and also protons can be polarized
  - Additional QED effects (radiative correction mainly)
  - Higher Twists QCD, lepton-photon non collinearity and other azimuthal modulated terms
  - Non SIDIS processes entering into the cuts (such as Vector Meson productions, target fragments)
5. the detector acceptance

The systematic errors on the relevant variables and the fluctuations of the experimental conditions cancel out in the asymmetry ratio. Residual effects due to target polarization drift and detector efficiency are minimized by the frequent target spin flip and the relatively short period of data taking. On the other hand, the high luminosity permit to analyze daily acquired subsets and to check their deviations; similar analysis can be exploited to estimate possible effects from unbalanced opposite beam spin states.

Moreover, the target polarization drift effects on asymmetry can be corrected as long as the target polarization is measured as discussed in the 6 GeV Transversity proposal [35].

Eventually single arm DIS events (which already takes into account the trigger efficiency), will be used as precise luminosity monitor and as a cross check of the beam luminosity monitor.

### 5.6.1 Target related effects

There are at least two correlated sources of errors:

- the small effective proton polarization in  $^3\text{He}$  results in a small offset in the asymmetries and can be controlled using the data from HERMES on the proton;
- bound neutrons: neutron distribution functions and hadron fragmentation are affected by the other bounded nucleons; the recent work ([30]) on the JLab kinematics shows that such effects are negligible once the above effective proton polarization is taken into account.

### 5.6.2 Random background

The random events entering the coincidence time window represent an additional source of dilution; in fact the background corrected asymmetry ( $A_C$ ) can be expressed by[29]:

$$A_C = \frac{N_T}{N_S}A_M - \frac{N_B}{N_S}A_B = \frac{1}{1 - f_B}A_M - \frac{f_B}{1 - f_B}A_B$$

where  $N_T$ ,  $N_S$  and  $N_B$  are the total, signal and background events,  $A_M$  and  $A_B$  are the measured (not background corrected) and background asymmetries and  $f_B = N_B/N_T = 1/(1 + SNR)$  is the background dilution factor, related to the Signal to Noise Ratio (SNR). The SNR is maximized by the small coincidence time window and the precise cut on vertex position (see section 3) and is expected to exceed 30.

### 5.6.3 Exclusive Vector Meson production

The fluctuation of a virtual photon into its hadron components and the subsequent interaction of these components with the nucleon may generate hadrons in the final state that represent an additional background to the SIDIS hadrons (see previous section 5.6.2). Such background can be described by the Vector Meson Dominance model as interaction of vector mesons ( $\rho^0$ ,  $\omega$  and  $\phi$ ) with the nucleon.

The contamination of pions from the vector mesons have been preliminary estimated using PYTHIA tuned to the HERMES data [31] and are reported as a function of  $x$  in figure 5.9. Detailed analysis [32] of the HERMES data (which suffers of higher contamination) demonstrates that the VM effects on the Collins and Sivers extraction is negligible.

Moreover, its influence can be investigated during the analysis increasing the upper cut on  $z$ , where the VM events are expected to be relevant.

### 5.6.4 Hadron Identification

The performance of the HERMES RICH detector that will be adapted to the SBS spectrometer has been deeply investigated in HERMES. Two reconstruction techniques (and mixture of them) has been used in the rather clean HERMES ring reconstruction: Inverse and Direct raytracing [18]. The latter one which is based on a mixture of analytic approximation and

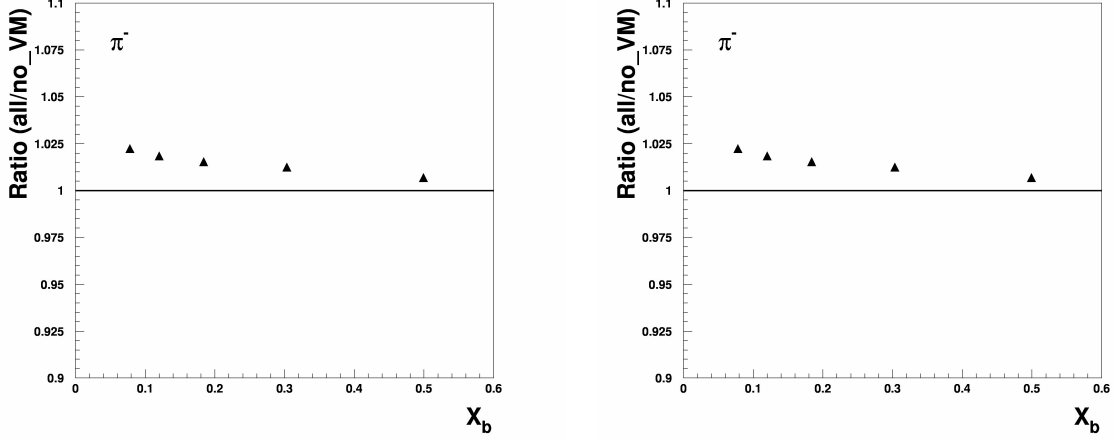


Figure 5.9: Pion contamination from Vector Meson processes

Monte Carlo simulation, is expected to work better in the expected higher ( $\sim 5\%$ ) occupancy of the proposed experiment, due to the fact that it is able to transparently handle multi tracks events. Misidentification of the hadron (especially Kaons due to the unfavored production ratio) can be represented as an additional (polarized) background (see section 5.6.2).

The estimate of the systematic uncertainties in the RICH identification can be carried on with low luminosity dedicated runs which produce clean pattern on the RICH (at the same level of HERMES). Once the clean events have been characterized, they will be cumulated to obtain the experimental higher occupancy.

### 5.6.5 Additional azimuthal modulated terms

The measured  $A_{UT}^{exp}$  depends on the cross section which in turn is the combination of several asymmetries (in addition to the considered Collins, Sivers and Pretzelosity) with their azimuthal modulations. Such additional terms may contribute to the  $A_{UT}$  for several reasons:

- higher twist terms of the above asymmetries (twist 4). They have the same azimuthal modulations. Their relatively strong  $(1/(Q^2)^2)$  dependence on  $Q^2$  will be investigated; this is one of the purpose of the two beam energy configurations.
- higher twist terms from the same beam (U)- target (T) configuration. They present different sinusoidal modulation and can be included in the fit and therefore their contributions estimated.
- terms from different target-photon relative spin configurations, due to the fact that the photon is not collinear with the lepton beam. This fact introduce addition terms (Lon-

gitudinal polarized photon - Transverse target and Unpolarized photon - Longitudinal target) contributing to the cross section. Their effects are expected to be negligible due to the small lepton- $\gamma$  angle.

- residual asymmetries from the unpolarized target - unpolarized beam can in principle produce some systematic effects. They present  $\cos$  modulations and their effects (expected to be negligible as in HERMES, [29]) can be estimated including them in the fit for the extraction of the other asymmetries.

### 5.6.6 Acceptance effects

The extraction of the asymmetries requires that different sets of data from the same sparse acceptance regions are combined together. Moreover, the extracted asymmetries are integrated in one or more kinematic variables on which the asymmetries depend.

Coverage of the full Sivers and Collins azimuthal angles is a prerequisite of the proposed experiment and is largely fulfilled as presented in Figs. 5.7 and 5.8.

Further reduction of the acceptance effects seems to be achievable with a new method of extraction [34, 29] based on unbinned Maximum Likelihood fit of the measured data with a probability density function (PDF) containing the target asymmetries; the fitted parameters are the coefficient of a Taylor expansion in the relevant kinematic variables. Once the parameters have been retrieved, the PDF is folded with the well know unpolarized Born cross section to obtain the asymmetries. The obtained moments is expected to correspond to those extracted from an ideal  $4\pi$  detector.

### 5.6.7 Study of additional systematics in the analysis

Other effects of the experimental apparatus will be investigated using the standard method of the “fake asymmetry” extracted from randomly assigning the target spin state to the data (both from production and calibration runs).

## 5.7 $A_{UT}$ Predictions

Figures 5.10 and 5.11 (adapted from fig. 1.5 and 1.6) show the pions projected errors of the proposed measurements on the Collins and Sivers asymmetries respectively, compared to the HERMES most recent (and unique) 2-dimensional data [33], for a single  $0.4 < z < 0.5$  bin for  $\pi^+$  and  $\pi^-$ . Accuracy improvements and extension of the  $x$  range toward higher  $x$  is evident.

The other  $z$  and  $x$  bins presented in the above tables (section 5.4) show similar behavior and are omitted.

Kaon projected error are presented in figures 5.12 and 5.13 for  $z$  and  $P_{\perp}$  integrated Collins and Sivers asymmetry respectively. They are compared to the preliminary HERMES data. We expect to proceed to a 2D grid extraction of these asymmetries as described in the previous sections.

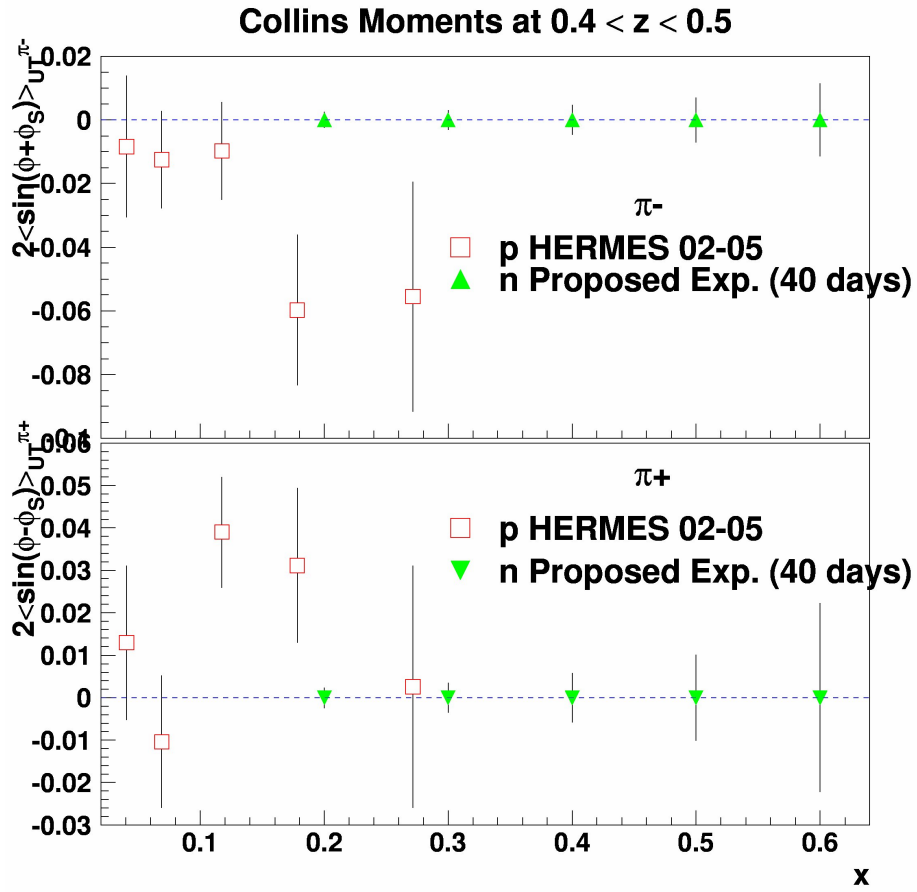


Figure 5.10: Projected statistical errors on neutron Collins moments from pions of the proposed experiment and  $x$  range, compared to the recent proton HERMES data [33] for  $0.4 < z < 0.5$  bin.

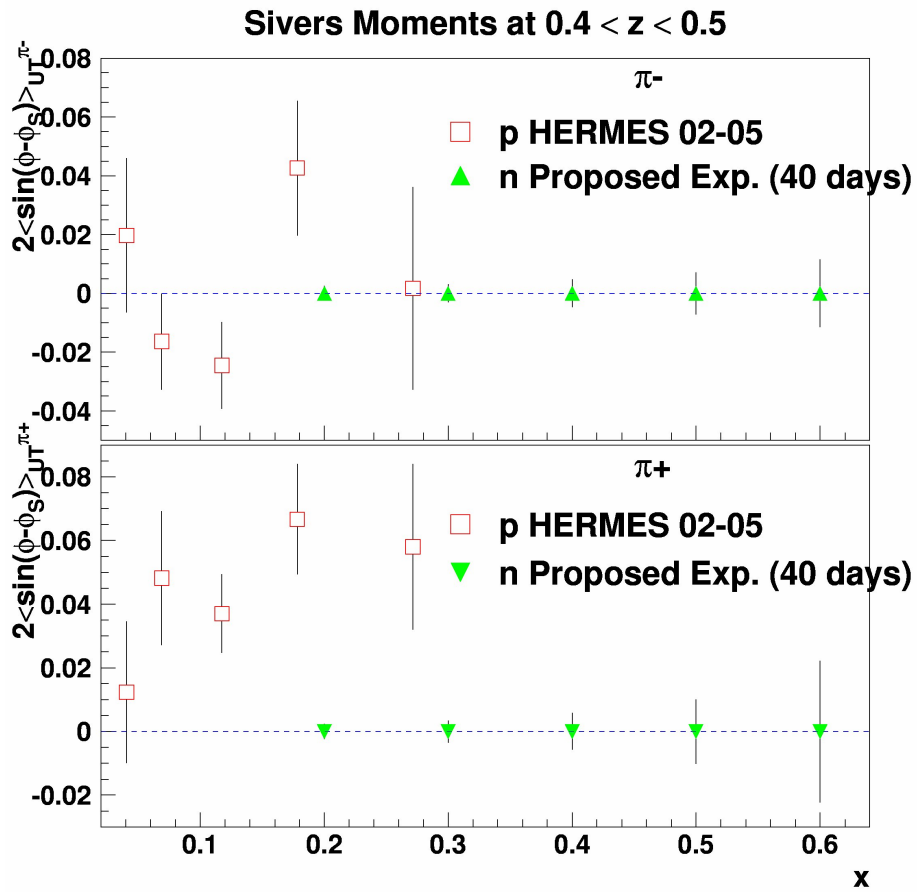


Figure 5.11: Projected statistical errors on neutron Sivers moments from pions of the proposed experiment and  $x$  range, compared to the recent proton HERMES data [33] for  $0.4 < z < 0.5$  bin.

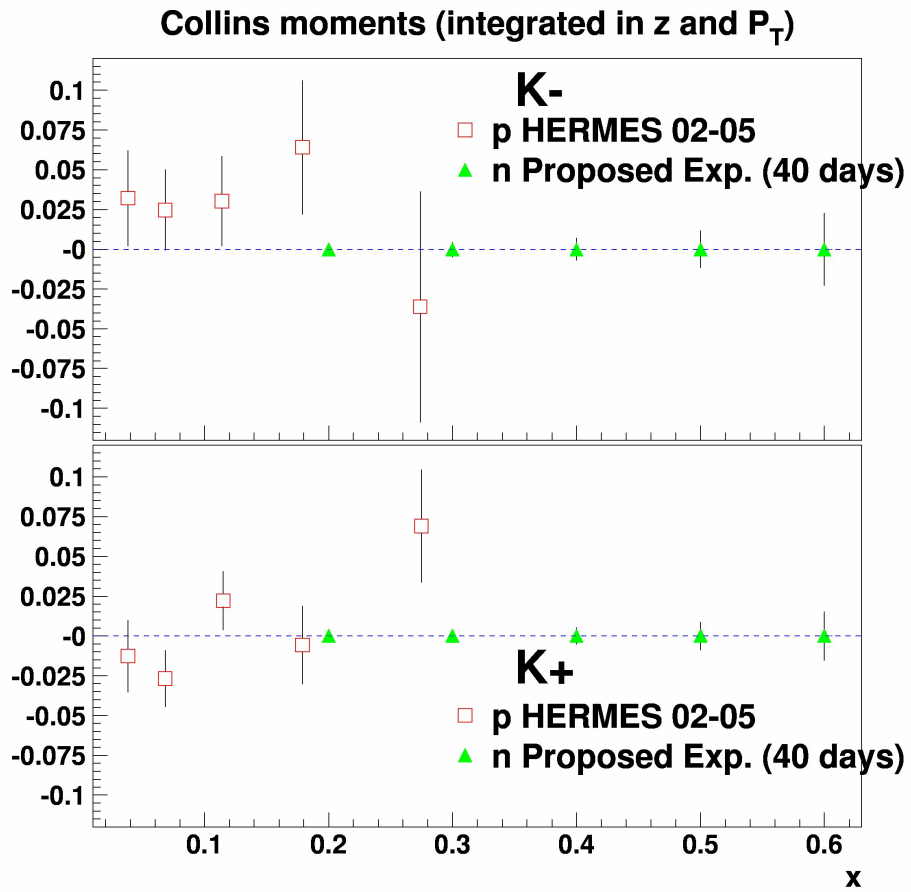


Figure 5.12: Projected statistical errors on neutron Collins moments from kaons of the proposed experiment versus  $x$ , compared to preliminary data from proton HERMES [29] integrated over  $z$  and  $P_{\perp}$ .

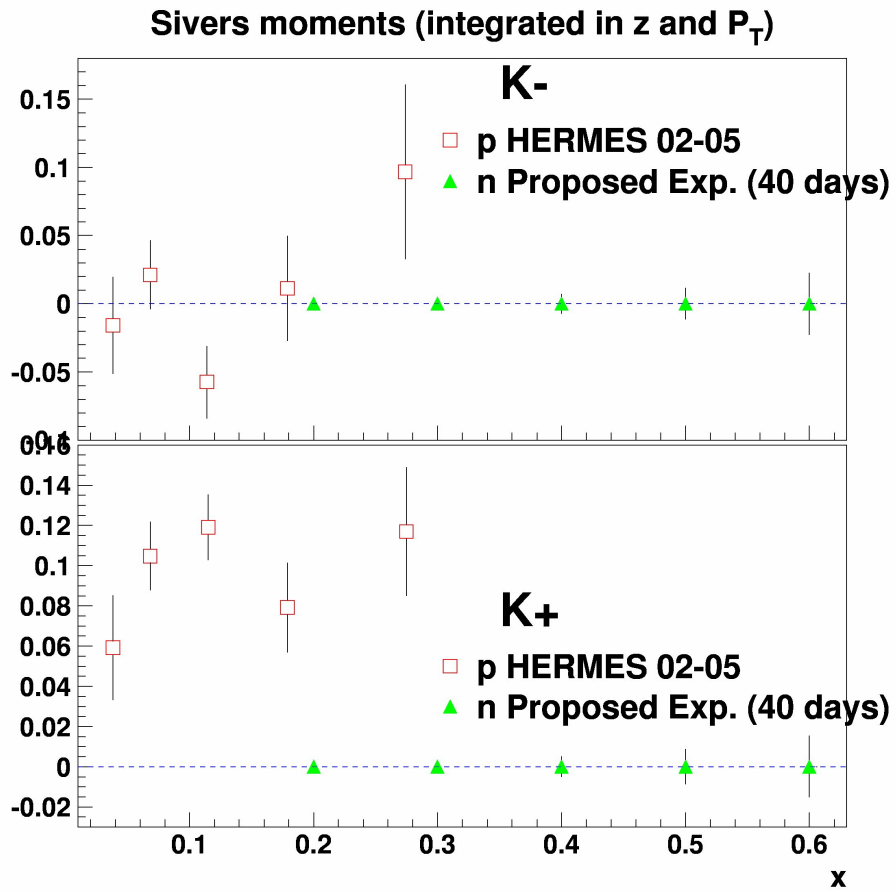


Figure 5.13: Projected statistical errors on neutron Sivers moments from kaons of the proposed experiment versus  $x$ , compared to preliminary data from proton HERMES [29] integrated over  $z$  and  $P_{\perp}$ .

# Chapter 6

## Summary

We have developed a SIDIS proposal with the Super Bigbite spectrometer (SBS) as the hadron arm, the BigBite spectrometer as the electron arm, and a high-luminosity polarized  $^3\text{He}$  target. A measurement of the proton form factor ratio using SBS was approved by PAC32, which underlined in its report the interest in further proposals that would use SBS, especially in SIDIS physics.

The design approach in our experiment uses a scheme that has worked very well in previous fixed-target experiments with a high-energy beam: HERMES and COMPASS. Specifically, we use an open-geometry dipole spectrometer at a small angle with respect to the beam. The key difference in our proposed experiment is very high luminosity, made possible in part by major advances in polarized  $^3\text{He}$  target technology, some of which were specifically aimed at facilitating the SBS physics program. Also critical to making use of this luminosity is the use of GEM technology for high-rate high-resolution tracking, and advanced RICH technology for particle ID.

The experimental results will include:

- Improved knowledge of the Collins and Sivers neutron asymmetries (by a factor of 10 with respect to the best data on the proton) for  $\pi^+$  and  $\pi^-$  electroproduction in the DIS regime.
- Extraction of the Collins and Sivers neutron asymmetries in a 2-dimensional grid for  $K^+$  and  $K^-$  electroproduction in the DIS regime.
- Accurate values of pion asymmetries up to  $x=0.6$  and  $z=0.65$ .
- The first accurate evaluation of  $Q^2$  dependence of the Collins and Sivers asymmetries, including reasonably fine binning in Bjorken  $x$ .

Data taking will occur at two electron beam energies, 8.8 and 11 GeV, which will facilitate studying the  $Q^2$  dependence of the SIDIS asymmetries. We will have excellent azimuthal coverage through the use of multiple target polarization directions, all of which will be transverse to the beam direction.

The responsibility for the construction of most major elements of the SBS spectrometer has already been assumed by various members of the form-factor collaboration. The only

element of the SBS that will be added specially for the SIDIS experiment is a RICH detector, for which we will adapt the HERMES RICH detector (presently in the storage at UVA). Since the polarized  $^3\text{He}$  target is virtually identical to the target that will be used for proposed 12 GeV Hall A GEN experiment, this proposal does not represent a huge incremental increase to the SBS program in terms of equipment.

**Requested Beam Time** The next table summarize the beam time requests.

	Time (day)
Production run at $E = 11$ GeV	40
Production run at $E = 8.8$ GeV	20
Calibration Runs	2
Target maintenance and configuration changes	2
<b>Total</b>	<b>64</b>

Productions runs have been presented in the previous sections. Calibration runs include measurements with the reference cell (unpolarized) and optics calibration targets devoted to background characterization and detector checks and tuning (such as the above mentioned RICH low luminosity runs).

We expect the new polarized target will require similar (or smaller) maintenance then the current polarized  $^3\text{He}$ . As long as possible, non production operations will be performed during the scheduled beam down time.

## Appendix A

# Collaboration responsibilities

The following is a list of personnel from the institutions and their intended contributions to the proposed experiment:

- The UVa group will take responsibility for the construction and operation of the high-polarization high-luminosity  $^3\text{He}$  target, which is also a major part of a new GEN proposal to this PAC. The UVa group will also take responsibility for the reconfiguration of the GEM-based tracker in Super Bigbite Spectrometer and its operation. We note that the UVa group is applying for a significant NSF MRI grant related to the Super Bigbite Spectrometer.
- The CMU group will use will use their expertise in calorimeters to implement the hadron calorimeter and the beam line magnetic shielding, both of which are also required in GEP5 experiment E12-07-109. The source of funding for this group is DOE.
- The INFN group is committed to providing a reconfigured GEM tracker for BigBite, as well as taking the lead in its operation and support. They will also have major role in the implementation of the RICH detector. The source of funding for this group is INFN.
- The Hall A collaborators will take responsibility for the infrastructure associated with the 48D48 magnet, which will be used in both this and the three SBS-related Form-Factor experiments.

The UVa group has played a leading role in advancing polarized  $^3\text{He}$  target technology, and has recently focused on demonstrating the necessary steps that will enable the implementation of a very-high-luminosity target. In addition to alkali-hybrid technology and the use of spectrally narrowed lasers, which have already delivered major improvements in performance in running experiments, the UVa group has recently demonstrated the use of “convection-driven” cells that make it possible to tolerate high beam currents without excessive loss of polarization. The UVa group has also recently developed a major new tracker system for the BigBite spectrometer, and will submit an MRI proposal to the NSF for the construction of a GEM-based tracker for SBS.

The CMU group has made major contributions to JLab parity experiments in both Halls A and C, the Hall A GEN experiment (E02-013), and many experiments in Hall B. Together with the William and Mary group, CMU has taken responsibility to prepare much of the hadron calorimeter elements and their implementation in time for the experiment around 2014.

The INFN groups at JLab have recently merged into a single, stronger Italian collaboration. The collaboration has also gained additional members, doubling its original size to a total of about 30 researchers. One of the 3 main physics objectives of the collaboration program is devoted to the study of the spin structure of the nucleon. The source of research funding for this group is the INFN. Members of the INFN group had a leading role in the design, construction and operation of the HERMES RICH and of the Hall A RICH. About 1/3 of the members are directly involved in the development of the SBS project. In fact, the program of experiments with the SBS spectrometer got a strong support of INFN, which already approved the development of the First Tracker of SBS, and funded 250 keuro for the prototyping.

The Glasgow group intends to work on similar GEM-based detectors for the PANDA experiment and will share their results in hardware design and readout software with this experiment, effectively contributing several FTE's.

The Florida International University also intends to contribute to the development of a GEM-based tracker at least 1 FTE and put a graduate PhD thesis student in this experiment.

# Bibliography

- [1] S.D. Bass, *Reviews of Modern Physics*, **77**, 2005.
- [2] J.C. Collins, *Nucl. Phys. B* **396**, 161 (1993).
- [3] J.C. Collins and A. Metz, *Phys. Rev. Lett.* **93**, 252001 (2004).
- [4] D.W. Sivers, *Phys. Rev.* **41**, 83 (1990); **43**, 261 (1991).
- [5] M. Burkardt, *Phys. Rev.* **66**, 114005 2002.
- [6] M. Burkardt, arXiv:0709.2966v3 [hep-ph] (2008).
- [7] G.A. Miller, *Phys. Rev. Lett.* **99**, 112001 (2007).
- [8] C.E. Carlson and M. Vanderhaeghen, *Phys. Rev. Lett.* **100**, 032004 (2008).
- [9] A. Airapetian *et al.*, *Phys. Rev. Lett.* **94**, 012002 (2005).
- [10] V. Y. Alexakhin *et al.*, *Phys. Rev. Lett.* **94**, 202002 (2005).
- [11] G. Cates, N. Lyianage, B. Wojtsekhowski *et al.*, Measurement of the Neutron Electric Form Factor  $G_{En}$  at High  $Q^2$ , JLab experiment E02-013.
- [12] Conceptual Design Report (CDR) for The Science and Experimental Equipment for The 12 GeV Upgrade of CEBAF, [http://www.jlab.org/div\\_dept/physics\\_division/GeV](http://www.jlab.org/div_dept/physics_division/GeV)
- [13] <http://hallaweb.jlab.org/12GeV/SuperBigBite/>
- [14] C.F. Perdrisat, L. Pentchev, E. Cisbani, V. Punjabi, B. Wojtsekhowski *et al.*, Large Acceptance Proton Form Factor Ratio Measurements at 13 and 15  $(\text{GeV}/c)^2$  Using Recoil Polarization Method, JLab experiment E12-07-109.
- [15] P. Degtyarenko, private communication (2007).
- [16] F. Sauli, *Nucl. Instr. Meth.* **A386** (1997) 531.
- [17] G. Cates, private communication.
- [18] N. Akopov *et al.*, *Nucl. Instr. Meth.* **A479** 511 (2002).
- [19] D.E. Wisner, Ph.D. Thesis, University of Wisconsin-Madison (1977) (unpublished).

- [20] E. Babcock, B. Chann, T.G. Walker, W.C. Chen and T.R. Gentile, *Phys. Rev. Lett.* **96**, 083003 (2006).
- [21] K.D. Bonin, T.G. Walker and W. Happer, *Phys. Rev. A* **37**, 3270 (1988).
- [22] K.P. Coulter, A.B. McDonald, G.D. Cates, W. Happer and T.E. Chupp, *Nuc. Inst. and Meth. in Phys. Res.* **A276**, 29 (1989).
- [23] A. Deninger, W. Heil, E.W. Otten, M. Wolf, R.K. Kremer and A. Simon, *Eur. Phys. J. D* **38**, 439 (2006).
- [24] N.R. Newbury, A.S. Barton, P. Bogorad, G.D. Cates, M. Gatzke, B. Saam, L. Han, R. Holmes, P.A. Souder, J. Xu, and D. Benton, *Laser Polarized Muonic Helium*, *Phys. Rev. Lett.* **67**, 3219 (1991).
- [25] A. Bacchetta *et al.*, “Semi-inclusive deep inelastic scattering at small transverse momentum”, *JHEP02* (2007) 093.
- [26] H.L. Lai *et al.*, hep-ph/9903282.
- [27] deFlorian *et al.*, *Phys. Rep.* **D 75** 114010 (2007) and hep-ph/0703242v1, 22 Mar 2007
- [28] A. Airapetian *et al.*, *Phys. Rev. D* 75 (2007) 011103(R), hep-ex/0605108; B. Maiheu, “Hadronization in electron - proton scattering at HERMES”, PHD Thesis, Universiteit Gent, March 2006
- [29] L.L. Pappalardo, “Transverse spin effects in polarized semi inclusive deep inelastic scattering”, PHD Thesis, Ferrara 2008, available at <http://www.fe.infn.it/u/pappalardo/thesis.pdf>
- [30] S. Scopetta, “Sivers function an Constituent Quark Model”, talk given at the 2008 Transversity Workshop, Ferrara, available at <http://www.fe.infn.it/transversity2008/>
- [31] L.L. Pappalardo and M. Contalbrigo, private communication
- [32] U. Elschenbroich, “Transverse Spin Structure of the Proton Studied in Semi-Inclusive DIS”, DESY-THESIS-2006-004, (2006).
- [33] M. Contalbrigo, “Transverse Spin Physics at HERMES”, presented at SPIN 2008, available at [http://www.faculty.virginia.edu/spin2008/scientific\\_program.html](http://www.faculty.virginia.edu/spin2008/scientific_program.html)
- [34] A. Miller, “Extracting azimuthal Fourier moments from sparse data”, presented at the HERMES Transversity Week, Gent, (2006)
- [35] J-P. Chen, X. Jiang, J-C. Peng, JLab Hall A experiment E06-010, E. Cisbani, H. Gao, X. Jiang, Hall A experiment E06-011
- [36] A. Bacchetta *et al.*, *Phys. Rev. D* 70, 117504 (2004)
- [37] H. Avakian *et al.*, “Pretzelosity distribution function”, arXiv/hep-ph:0808.3982, 2008

- [38] COMPASS Collaboration, “Collins and Sivers Transverse Spin Asymmetries for Pions and Kaons in Deuterons”, CERN.PH-EP/2008-002
- [39] H. Wollny, “Transverse spin effects at COMPASS”, presented at SPIN 2008, available at [http://www.faculty.virginia.edu/spin2008/scientific\\_program.html](http://www.faculty.virginia.edu/spin2008/scientific_program.html)
- [40] L. Pappalardo, “Measurement of Collins and Sivers asymmetries at HERMES”, talk given at the 2008 Transversity Workshop, Ferrara, available at <http://www.fe.infn.it/transversity2008/>
- [41] H. Avakian, ”TMD measurement at CLASS6 and CLAS12”, talk presented at the TRANSVERSITY 2008 workshop, 2008, available at <http://www.fe.infn.it/transversity2008/>
- [42] M. Anselmino *et al.*, “Transversity and Collins functions from SIDIS and e+e- data”, Phys. Rev. D75, 054032 (2007), arXiv:hep-ph/0701006 and arXiv:hep-ph/0807.0173v1 (2008)
- [43] M. Anselmino *et al.*, “Sivers Effect for Pion and Kaon Production in Semi-Inclusive Deep Inelastic Scattering”, arXiv/hep-ph:0805.2677
- [44] R. De Leo, “Long-term operational experience with the HERMES RICH detector”, talk presented at RICH 2007, Trieste, Italy; available at: <http://rich2007.ts.infn.it/>